catalysts

MDPI

Review

Carbon Nitride-Based Catalysts for Photocatalytic NO Removal

Sheng Wang [1], Fu Chen [1,2,*], Xiyao Niu [3] and Huagen Liang [3,*]

[1] State Key Laboratory of Low-Carbon Smart Coal-Fired Power Generation and Ultra-Clean Emission, China Energy Science and Technology Research Institute Co., Ltd., Nanjing 210023, China
[2] School of Public Administration, Hohai University, Nanjing 211100, China
[3] Carbon Neutrality Institute, China University of Mining and Technology, Xuzhou 221008, China
* Correspondence: chenfu@hhu.edu.cn (F.C.); lianghg@cumt.edu.cn (H.L.)

Abstract

Nitrogen oxides (NO_x) are major atmospheric pollutants, and their escalating emissions, driven by rapid economic development and urbanization, pose a severe threat to both the ecological environment and human health. Conventional denitrification technologies are often hampered by high costs, significant energy consumption, and stringent operational conditions, making them increasingly inadequate in the face of tightening environmental regulations. In this context, photocatalytic technology, particularly systems based on graphitic carbon nitride (g-C_3N_4), has garnered significant research interest for NO_x removal due to its visible-light responsiveness, high stability, and environmental benignity. To advance the performance of g-C_3N_4, numerous modification strategies have been explored, including morphology control, elemental doping, defect engineering, and heterostructure construction. These approaches effectively broaden the light absorption range, enhance the separation efficiency of photogenerated electron-hole pairs, and improve the adsorption and conversion capacities for NO_x. Notably, constructing heterojunctions between g-C_3N_4 and other materials (e.g., metal oxides, noble metals, metal–organic frameworks (MOFs)) has proven highly effective in boosting catalytic activity and stability. Furthermore, the underlying photocatalytic mechanisms, encompassing the generation and migration pathways of charge carriers, the redox reaction pathways of NO_x, and the influence of external factors like light intensity and reaction temperature, have been extensively investigated. From an application perspective, g-C_3N_4-based photocatalysis demonstrates considerable potential in flue gas denitrification, vehicle exhaust purification, and air purification. Despite these advancements, several challenges remain, such as limited solar energy utilization, rapid charge carrier recombination, and insufficient long-term stability, which hinder large-scale implementation. Future research should focus on further optimizing the material structure, developing greener synthesis routes, enhancing catalyst stability and poison resistance, and advancing cost-effective engineering applications to facilitate the practical deployment of g-C_3N_4-based photocatalytic technology in air pollution control.

Keywords: nitrogen oxides; photocatalysis; graphitic carbon nitride; modification strategy; air purification

check for updates

Academic Editor: Edward G. Gillan

Received: 2 October 2025
Revised: 25 October 2025
Accepted: 28 October 2025
Published: 3 November 2025

Citation: Wang, S.; Chen, F.; Niu, X.; Liang, H. Carbon Nitride-Based Catalysts for Photocatalytic NO Removal. *Catalysts* **2025**, *15*, 1043. https://doi.org/10.3390/catal15111043

Copyright: © 2025 by the authors. Licensee MDPI, Basel, Switzerland. This article is an open access article distributed under the terms and conditions of the Creative Commons Attribution (CC BY) license (https://creativecommons.org/licenses/by/4.0/).

1. Introduction

Nitrogen oxides (NO_x) are major atmospheric pollutants originating from a variety of sources, such as vehicle emissions, industrial combustion, agricultural activities, and natural phenomena. In recent years, China's sustained economic growth and rapid urbanization have contributed to increasing NO_x emissions, which significantly degrade

air quality and present considerable challenges to improving atmospheric environmental conditions. Vehicle exhaust constitutes a particularly critical source, with the growing number of motor vehicles directly driving up total NO_x emissions. Statistics indicate that vehicular exhaust contributes to over 40% of the national NO_x emissions in China. This issue is further aggravated by urban traffic congestion, leading to prolonged vehicle idling and consequently higher NO_x release. Additionally, the industrial sector represents another major contributor to NO_x emissions. Energy-intensive industries, such as thermal power generation, steel production, and cement manufacturing, emit substantial amounts of NO_x during fossil fuel combustion. Although the Chinese government has strengthened regulations on industrial emissions and promoted denitrification technologies, the overall NO_x output remains high due to the large scale of industrial operations and the prevailing energy structure. Agricultural practices and natural processes also add to environmental NO_x levels. Fertilizer application and open straw burning are notable agricultural sources, while natural events such as volcanic eruptions and forest fires can introduce significant quantities of NO_x into the atmosphere. Although these sources are often geographically dispersed, they can substantially impact local air quality under specific conditions. The environmental and health impacts of NO_x cannot be overlooked. NO_x plays a key role in the formation of photochemical smog and acid rain, and enhances atmospheric oxidation capacity, thereby aggravating complex air pollution problems. In response, the government has implemented various countermeasures, including stricter vehicle emission standards, improved industrial denitrification efficiency, and promotion of clean energy alternatives. However, NO_x emission control still faces technical, economic, and managerial obstacles. Therefore, there is an urgent need for enhanced scientific research investment and policy support to effectively mitigate NO_x pollution [1].

Currently, methods such as physical adsorption [2],chemical absorption [3], selective catalytic reduction [4], and selective non-catalytic reduction [5] are widely employed for removing high-concentration (ppm-level) NO_x. However, conventional denitrification techniques often entail high costs, complex operations, risks of ammonia leakage, and potential secondary pollution, making them inadequate to meet the growing demand for economical, safe, and efficient emission control technologies [6]. Recently, photocatalysis has attracted considerable attention in environmental remediation due to its high efficiency, low cost, and minimal pollution risk. It is regarded as one of the most promising and environmentally friendly strategies for NO_x removal [7–9]. The efficiency and selectivity of photocatalytic NO_x conversion are closely related to the type, structure, and physicochemical properties of the photocatalyst employed [10]. A variety of ingeniously designed and highly effective photocatalysts, such as TiO_2 [11] and bismuth-based oxides [12,13], have been successively developed for photocatalytic NO_x removal.

Graphitic carbon nitride (g-C_3N_4), a typical non-metallic semiconductor, offers numerous advantages including facile synthesis, structural stability, suitable band gap, low cost, and visible-light responsiveness. These properties render it a promising candidate in the field of photocatalysis [14,15]. However, bulk g-C_3N_4 exhibits suboptimal photocatalytic performance in NO removal due to several intrinsic drawbacks: poor specific surface area, restricted light absorption efficiency, rapid recombination of photogenerated carriers, and insufficient adsorption/activation sites [16,17]. In light of recent research progress, this review provides a comprehensive overview of g-C_3N_4-based photocatalysts for NO oxidation. It systematically examines how various modification strategies, such as morphology control, structural optimization, vacancy engineering, elemental doping, surface modification, and heterostructure construction, influence the photocatalytic performance. Moreover, the review discusses how microstructural features and photoelectric properties affect the adsorption and activation of NO on g-C_3N_4-based catalysts, in relation to their efficiency

and selectivity in photocatalytic NO oxidation. Finally, current challenges in this field are summarized, and future research directions are proposed to guide the development of more efficient g-C_3N_4-based photocatalysts for NO removal.

2. NO Photocatalytic Removal Mechanism

The photocatalytic removal of nitrogen monoxide (NO) primarily involves three pathways: oxidation, direct decomposition, and selective reduction [18]. Photocatalytic decomposition refers to the direct dissociation of NO into nitrogen (N_2) and oxygen (O_2) on the catalyst surface. As this process requires no additional oxidants or reductants, it represents the simplest denitrification route and minimizes the risk of secondary pollution. However, both the cleavage of the N=O bond and the formation of the N≡N bond involve considerable energy barriers [19]. Moreover, existing photocatalysts generally exhibit low activity and selectivity toward this reaction, resulting in slow decomposition rates that are currently impractical for large-scale application. Consequently, studies on direct photocatalytic decomposition of NO remain limited.

Photocatalytic selective reduction (photo-SCR) resembles conventional selective catalytic reduction; it employs light energy to assist reductants such as ammonia (NH_3), hydrogen (H_2), carbon monoxide (CO), or hydrocarbons in converting NO to N_2 at relatively low temperatures (<200 °C), thereby significantly reducing energy consumption [20]. However, this method carries risks of NH_3 or CO leakage, which can cause secondary pollution, and poses challenges under real outdoor lighting conditions. The photo-SCR process is also relatively complex and demands stringent equipment specifications.

In contrast, photocatalytic oxidation utilizes active oxygen species generated during illumination to efficiently oxidize NO into nitrate (Figure 1). This approach is simple to operate and requires only minimal process equipment [21]. As a result, current research efforts are predominantly focused on photocatalytic NO oxidation under ambient conditions (room temperature and atmospheric pressure).

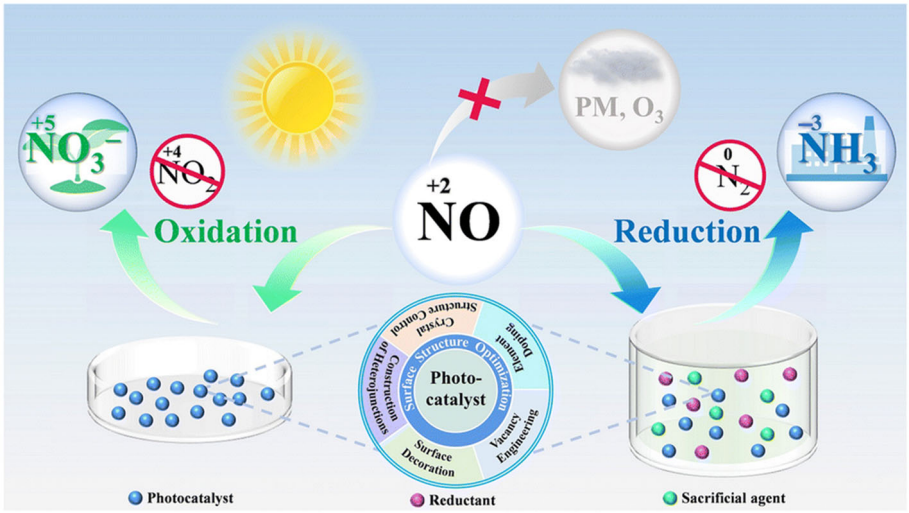

Figure 1. Illustration of the complete photocatalytic oxidation and reduction of NO for toxic by-product inhibition [21]. Copyright 2014, Royal Society of Chemistry.

A common prerequisite across all these photocatalytic NO removal routes is the generation of photogenerated electrons and holes [22]. Under light irradiation whose energy (hν) exceeds the band gap of the semiconductor (e.g., ~2.7 eV for g-C_3N_4), electrons (e^-) in the valence band (VB) are excited to the conduction band (CB), leaving holes (h^+) in the VB and forming electron–hole pairs. These charge carriers then migrate to the

semiconductor surface, where they participate in redox reactions with adsorbed species such as O_2, H_2O, and NO, yielding various reactive oxygen species (e.g., •OH, $\bullet O_2^-$, and $^1O_2$). These active species, together with photogenerated holes, collectively oxidize NO into intermediates like HNO_2 and NO_2, which are ultimately converted into nitrate (Equations (1)–(12)).

Due to differences in carrier mobility—electrons generally migrate more readily than holes—recombination during migration significantly affects overall efficiency. The overall photocatalytic efficiency is thus contingent upon maximizing the proportion of photogenerated carriers that successfully reach the surface and participate in redox reactions prior to recombination. Consequently, enhancing separation efficiency between photogenerated electrons and holes emerges as a critical factor for improving photocatalytic NO removal efficacy [23]. Furthermore, it is noteworthy that intermediate NO_2 possesses toxicity levels approximately 8.48 times greater than those associated with NO, therefore, effectively inhibiting its generation represents a key challenge within photocatalytic oxidation processes targeting NO [24].

$$\text{Photocatalyst} + h\nu \rightarrow e^- + h^+ \quad (1)$$

$$H_2O + h^+ \rightarrow H^+ + \bullet OH \quad (2)$$

$$O_2 + e^- \rightarrow \bullet O_2^- \quad (3)$$

$$O_2 + \text{energy} \rightarrow {}^1O_2 \quad (4)$$

$$NO + \bullet OH \rightarrow HNO_2 \quad (5)$$

$$HNO_2 + \bullet OH \rightarrow NO_2 + H_2O \quad (6)$$

$$NO_2 + \bullet OH \rightarrow HNO_3 \quad (7)$$

$$NO + \bullet O_2^- \rightarrow NO_3^- \quad (8)$$

$$2NO + \bullet O_2^- + 3e^- \rightarrow 2NO_2 \quad (9)$$

$${}^1O_2 + NO \rightarrow NO_3^- \quad (10)$$

$$3NO_2 + 2OH^- \rightarrow 2NO_3^- + NO + H_2O \quad (11)$$

$$HNO_3 \rightarrow H^+ + NO_3^- \quad (12)$$

Different active species can lead to distinct NO oxidation pathways and selectivity outcomes. For instance, Shi et al. [25] reported that the strong exciton effect in BiOBr nanosheets promotes O_2 activation to form singlet oxygen ($^1O_2$), which has relatively weak oxidation capacity and only partially oxidizes NO to the more toxic NO_2. Through surface boronation, an interlaced band alignment from bulk to surface was constructed in BiOBr, facilitating exciton dissociation into free carriers. Simultaneously, in situ generated oxygen vacancies captured electrons and promoted the single-electron reduction of O_2 to form superoxide radicals ($\bullet O_2^-$), which possess stronger oxidation ability and drive the deep oxidation of NO to nitrate.

The presence and contribution of various active species can be qualitatively and quantitatively assessed through radical scavenging experiments [26] and electron spin resonance spectroscopy (ESR) [27]. Furthermore, in situ characterization techniques [28] such as diffuse reflectance infrared fourier transform spectroscopy (DRIFTS), X-ray photoelectron spectroscopy (XPS), transmission electron microscopy (TEM), and X-ray absorption fine structure (XAFS) can be employed to elucidate the adsorption/activation processes of reactant molecules on catalyst surfaces, as well as to track molecular- or atomic-level changes

in surface properties and microstructure. Such analyses help clarify the specific pathways and underlying mechanisms of photocatalytic NO oxidation.

3. Optimization Strategies for G-C_3N_4

The practical application of g-C_3N_4 is significantly constrained by its limited light absorption efficiency and inadequate separation of photogenerated carriers. To address these challenges, various strategies, such as morphological engineering, defect engineering, element doping, surface modification/functionalization, and heterostructure construction, have been developed to enhance its photocatalytic performance. The fundamental principles and recent progress in these approaches are detailed in the following sections.

3.1. Morphological Engineering and Surface Modification

The photocatalytic activity of g-C_3N_4 is strongly influenced by its morphology, particle size, specific surface area, and pore structure [29]. Bulk g-C_3N_4 typically exhibits a low specific surface area due to the stacking and aggregation of nanosheets, which constrains its catalytic performance. Modulating the morphology and microstructure of g-C_3N_4 can effectively increase the specific surface area, adjust the energy band structure, provide additional active sites, enhance charge separation and surface reactions, thereby improving light utilization efficiency.

Wu et al. [30] coupled hollow porous carbon nitride nanospheres (HCNS) with reduced graphene oxide (rGO) to prepare HCNS/rGO composite (as illustrated in Figure 2), which achieved a 64% removal rate for low-concentration NO (~600 ppb) in air under visible light. The photocatalytic membrane prepared by loading HCNS/rGO onto porous carbonized polymer nanofibers retained high photocatalytic efficiency. The hollow spherical architecture of HCNS enlarges the reaction interface and enhances light absorption, while the incorporation of rGO promotes electron transfer and charge separation, synergistically boosting photocatalytic activity.

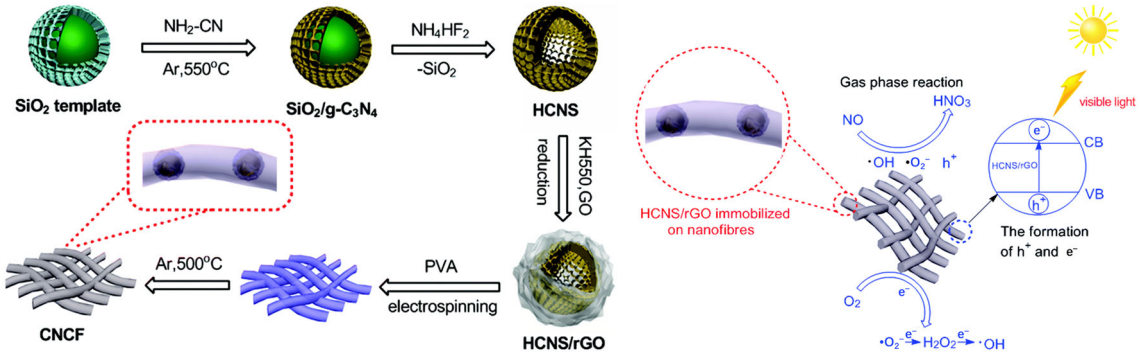

Figure 2. Synthesis process of HCNS/rGO/CNCF and the photocatalytic NO removal mechanism [30]. Copyright 2014, Royal Society of Chemistry.

Hydrothermal treatment of non-ordered g-C_3N_4 with NaOH solution can eliminate unstable domains, leading to in an increase in mesoporous structures and an eightfold expansion in specific surface area. This results in an 8.6-fold enhancement in the NO oxidation rate under visible light [31]. In dry NO atmospheres, the accumulation of intermediate products such as NO_2^- and NO_3^- on the catalyst surface temporarily diminishes the oxidation rate. However, these adsorbed species can be removed by water immersion, restoring the NO oxidation activity.

At 500 °C, KCl solid not only acts as a template but also interferes with the thermal polymerization of urea, thereby facilitating the one-step formation of a porous structure along with cyanide and hydroxyl groups (Figure 2) [32]. Compared with pure g-C_3N_4, the

cyanide and hydroxyl modified g-C_3N_4 shows a larger specific surface area, a narrower band gap, a more positive valence band potential, and improved migration and separation of photogenerated carriers, resulting in superior NO removal. Cyanide and hydroxyl groups promote spatial separation of HOMO and LUMO states and suppress electron–hole recombination. According to Wang et al. [33], yanide groups introduce intermediate energy levels that enhance light absorption, inhibit charge recombination, and promote $\bullet O_2^-$ generation. While NO adsorbed at cyanide sites can be oxidized by h^+ to toxic NO_2, hydroxyl groups facilitate further oxidation of NO_2 by $\bullet O_2^-$ to NO_3^-. In another study, Yi et al. [34] thermally exfoliated g-C_3N_4 in air to obtain O-modified g-C_3N_4. This process reduced the nanosheet thickness and increased the specific surface area, shortening the charge migration distance and providing abundant adsorption and reaction sites. The incorporated oxygen atoms act as electron traps, promoting charge migration and enhancing O_2/NO adsorption, thereby accelerating $\bullet O_2^-$ generation and improving NO activation and removal. Functional groups with strong electronegativity in g-C_3N_4 can act as electron traps and introduce new adsorption sites and activation sites, synergistically promoting the migration and separation of photogenerated carriers and enhancing the adsorption and activation of gas molecules.

Confinement of defective activated carbon (DAC) on g-C_3N_4 surfaces enhances O_2 adsorption and activation and creates new electron transport pathways, accelerating NO oxidation [35]. Under visible light, the NO oxidation efficiency was 2.1 times higher than that of pure g-C_3N_4. Similarly, modifications using graphene oxide [36], graphene quantum dots [37], reduced graphene oxide [38] and epitaxial graphene units [39] have been shown to significantly boost the photocatalytic activity of g-C_3N_4 for NO oxidation.

3.2. Doping Engineering

Incorporating single or multiple atoms into the g-C_3N_4 lattice is an effective strategy for tailoring its electronic structure and enhancing photocatalytic performance [40]. Doping can be classified by element type into non-metal doping and metal doping. Non-metal doping typically involves substituting carbon (C) or nitrogen (N) atoms in the g-C_3N_4 framework with elements such as boron (B), oxygen (O), sulfur (S), phosphorus (P), or halogens. Metal doping, on the other hand, usually entails either embedding metal atoms into the in-plane cavities of the triazine rings to form strong M-N_x coordination bonds, or intercalating metal cations between g-C_3N_4 layers to create bridging configurations. Furthermore, based on the number of doped elements, this approach can be categorized as single-element doping or multi-element co-doping. Table 1 summa rises the current developments in doped g-C_3N_4-based catalysts for the photocatalytic oxidation of NO.

Table 1. Summary of doped g-C_3N_4-based catalysts for the photocatalytic oxidation of NO.

Materials	Light Source	NO	Removal Rate	Reaction Time (min)	Ref.
C self-doped g-C_3N_4	150 W tungsten halogen lamp (λ > 420 nm)	500 ppb	56.77%	30	[41]
B-doped tubular g-C_3N_4	300 W Xe arc lamp (λ > 420 nm)	400 ppb	30.4%	30	[42]
S-doped holey g-C_3N_4 nanosheet	150 W visible LED lamp (λ > 400 nm)	600 ppm	53%	30	[43]
p-type g-C_3N_4	Xenon lamp (λ > 420 nm)	600 ppb	80%	30	[44]
Na-doped g-C_3N_4	visible LED lamp (λ > 420 nm)	550 ppb	55.8%	30	[45]
K-doped g-C_3N_4	150 W tungsten halogen lamp (λ > 420 nm)	500 ppb	41.93%	30	[46, 47]
Cs/Rb-doped g-C_3N_4	150 W tungsten halogen lamp (λ > 420 nm)	600 ppb	48.51%/51.11%	30	[48]
Group IIA ion-doped g-C_3N_4	Xenon lamp (λ > 420 nm)	600 ppb	62% (for Ba^{2+})	10	[49]
Sr-doped g-C_3N_4	300 W Xenon lamp (λ > 420 nm)	600 ppb	55%	9	[50]
Zn-doped g-C_3N_4	150 W metal halide lamp (λ > 420 nm)	600 ppb	49%	30	[51]

Table 1. *Cont.*

Materials	Light Source	NO	Removal Rate	Reaction Time (min)	Ref.
K^+, Cl^- ions co-doped g-C_3N_4	150 W tungsten halogen lamp (λ > 420 nm)	600 ppb	38.4%	30	[52]
O, Ba co-doped g-C_3N_4	150 W tungsten halogen lamp	500 ppb	56.4%	30	[53]
O, La co-doped g-C_3N_4	150 W tungsten halogen lamp	500 ppb	50.4%	30	[54]
Na^+, Li^+ ion co-doped g-C_3N_4	30 W visible LED lamp	600 ppb	82%	35	[55]

3.2.1. Non-Metal Doping

Non-metal element doping is a significant method for enhancing the performance of carbon nitride-based photocatalytic materials. It allows for precise adjustment of the band structure, improves light absorption, and promotes the separation of photogenerated electron-hole pairs, thereby boosting photocatalytic activity.

In g-C_3N_4 structures, C self-doping localizes electrons around the C atoms, which facilitates the electron-acceptance from NO atoms and thus activating NO (Figure 3). Furthermore, C self-doping can accelerate the separation of photogenerated electron-hole pairs and promote the generation of active free radicals [41].

Junaid et al. utilized density functional theory (DFT) calculations to investigate the photocatalytic reduction performance of N_2O using boron-doped carbon nitride nanosheets (B@g-C_3N_4) [56]. In the g-C_3N_4 hexagonal rings, B atoms preferentially substitute for C atoms, resulting in superior stability and catalytic activity compared to other doping sites. The B site acts as a pivotal center for N_2O activation: due to localized positive charge and spin density effects, N_2O molecules interacting with the B@g-C_3N_4 surface can spontaneously dissociate without external energy input. The adsorption energy of N_2O is more negative than that of CO, indicating that in flue gas environments containing both gases, N_2O will preferentially occupy the catalyst surface. The subsequent reaction between CO and adsorbed oxygen atoms effectively removes the O atoms bound to the B active sites, suggesting B@g-C_3N_4 as a promising catalyst for the simultaneous elimination of N_2O and CO.

B-doped tubular g-C_3N_4 exhibits a narrower band gap and enables multiple internal reflections of incident light, thereby enhancing light harvesting. Moreover, charge redistribution around the boron atoms induces electronic polarization, intensifying the internal electric field and promoting the separation of photogenerated carriers. The NO removal rate for B-doped tubular g-C_3N_4 reaches 30.4%, which is 1.5 times and 1.3 times higher than those of bulk g-C_3N_4 and undoped tubular g-C_3N_4, respectively [42]. Qi et al. [43] employed DFT calculations to study the effect of sulfur (S) doping on the adsorption and activation of O_2 and NO on g-C_3N_4. Their findings indicate that the interactions between NO/O_2 molecules and pristine g-C_3N_4 are weak, with minimal charge transfer. After S doping, electron transfer from g-C_3N_4 to adsorbed NO/O_2 is significantly enhanced, and the adsorption energy of O_2 increases markedly, optimizing charge transfer dynamics. Electron localization function (ELF) analysis reveals that S atoms alter the electronic distribution by localizing charges, which is beneficial for electron transfer and reactant activation. Adjacent carbon (C) atoms, due to their high electron density, can accept electrons from S atoms, extending the π-conjugated system, enhancing carrier separation efficiency, and enriching photogenerated electrons at the g-C_3N_4 surface, ultimately improving photocatalytic activity.

In photocatalytic oxidation, photogenerated holes often play a more critical role than electrons. p-Type semiconductors, where hole concentration significantly exceeds electron concentration, are generally more suitable for photocatalytic air pollutant removal compared to n-type semiconductors. Treating g-C_3N_4 nanosheets with HCl solution allows

Cl^- ions to fill the pores, effectively converting its semiconductor behavior from n-type to p-type, resulting in a 3.5-fold increase in photocatalytic NO oxidation activity [44]. The introduced Cl^- species create acceptor levels above the valence band maximum. These intermediate levels enhance visible light absorption, facilitate electron excitation, and suppress the recombination of photogenerated carriers. Furthermore, p-type g-C_3N_4 generates a greater number of holes, augmenting its capacity for NO oxidation.

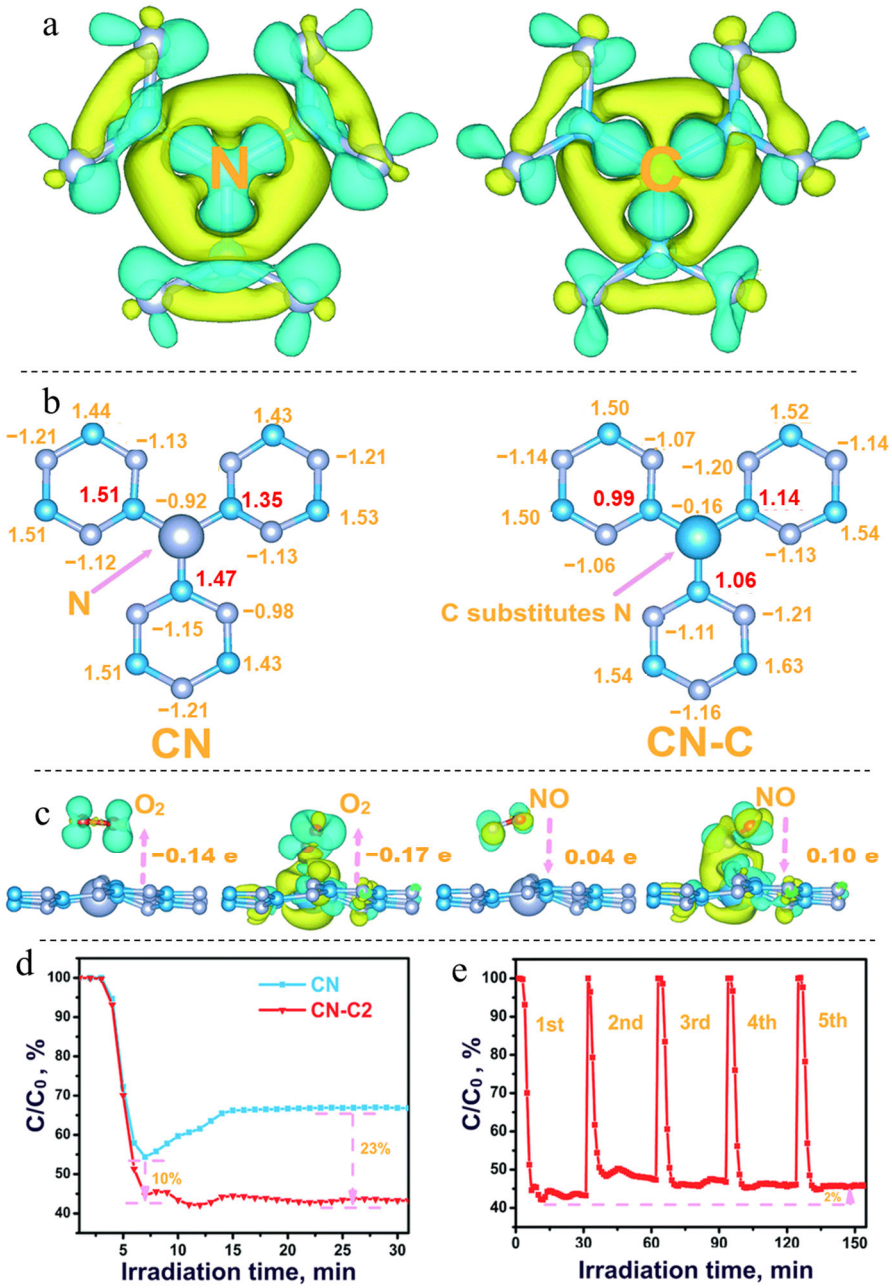

Figure 3. Charge difference distribution (**a**) and carried electrons (**b**) of pristine g-C_3N_4 and C self-doped g-C_3N_4, charge difference distribution of optimized O_2/NO adsorption on pristine g-C_3N_4 and C self-doped g-C_3N_4 (**c**); the photocatalytic NO_x removal performance of pristine g-C_3N_4 and C self-doped g-C_3N_4 (**d**); and cycling stability of C self-doped g-C_3N_4 (**e**) [41]. Copyright 2018, Royal Society of Chemistry.

3.2.2. Metal Doping

Metal-doped g-C_3N_4 has been widely explored to enhance photocatalytic activity and selectivity. Single-atom sodium (Na) doping increases the light absorption rate and

adsorption capacity of g-C_3N_4, facilitates carrier separation, and significantly elevates the NO removal efficiency from 36.8% to 52.5%, while simultaneously suppressing the formation of toxic NO_2 by-products (Figure 4) [45]. Electron localization function (ELF) analysis confirms that Na atoms occupy carbon sites within g-C_3N_4, forming N-Na-N bonds. Charge difference distribution analysis indicates electron transfer from Na to adjacent nitrogen atoms, activating N-C_3 motifs and generating an internal electric field between layers. This enhances lateral charge transfer and improves photocatalytic performance. It is generally accepted that Na atoms embed within the π-conjugated plane of g-C_3N_4. In contrast, larger alkali metal atoms such as potassium (K) [46,47] and cesium/rubidium (Cs/Rb) [48] tend to intercalate between g-C_3N_4 layers. This intercalation forms charge transfer bridges and channels, reducing electron localization and effectively separating charge carriers.

Zhou et al. [49] investigated the photocatalytic activity for NO removal of g-C_3N_4 doped with Group IIA (alkaline earth metal) ions (Mg^{2+}, Ca^{2+}, Sr^{2+}, and Ba^{2+}). These ions can form coordination bonds with nitrogen atoms on the triazine rings, causing structural distortion in g-C_3N_4 due to uneven forces. As the atomic number of the dopant increases, more coordination bonds form, leading to greater structural distortion. This distortion disrupts surface electron delocalization, inhibits surface carrier recombination, and the coordination bonds can also connect adjacent layers, functioning as interlayer electron channels that significantly enhance interlayer electron transfer. The structural distortion also increases the density of amino and imino groups, which serve as chemical adsorption sites for O_2 molecules. Compared to undoped g-C_3N_4, the distorted, doped g-C_3N_4 exhibits improved O_2 adsorption and activation capabilities, promoting the generation of more reactive oxygen species. Consequently, the NO removal efficiency of doped g-C_3N_4 increases with the atomic number of the Group IIA dopant. In another study, Zhou et al. [50] proposed that strontium (Sr) atoms can be incorporated into g-C_3N_4 via interlayer insertion, cavity filling, or substitution at triazine N or bridging N sites, suggesting the feasibility of multi-site doping from the surface to the bulk phase. Regardless of the doping mode, Sr incorporation effectively reduces the band gap of g-C_3N_4 and variably influences the adsorption and activation of reactant molecules. Notably, interlayer-inserted Sr enhances the separation and transfer of photogenerated charges by establishing a vertical charge channel between crystal planes. When Sr substitutes for N atoms, it facilitates O_2 activation to generate more $\bullet O_2^-$. Sr atoms occupying cavities within g-C_3N_4 enhance its ability to activate H_2O_2, increasing the yield of oxidizing •OH radicals and promoting deeper oxidation of NO to NO_3^-. These diverse doping strategies work synergistically to achieve efficient and comprehensive NO removal.

Zinc (Zn) single atoms can coordinate with three N atoms across two g-C_3N_4 layers, forming a Zn-N_3 bridging structure [51]. This structure significantly enhances visible light absorption, accelerates carrier transfer, and improves electron-hole separation. Moreover, Zn single atoms can promote the formation of a Zn-O_2-NO complex involving surface-adsorbed O_2 and NO molecules. This complex facilitates the direct oxidation of NO to nitrate with a reduced energy barrier, optimizing the reaction pathway. Consequently, this approach markedly increases the NO oxidation rate while minimizing NO_2 generation.

Hadi et al. [57] conducted DFT calculations to investigate the adsorption behavior of NO gas on pristine g-C_3N_4 and g-C_3N_4 modified with transition metal atoms (TM = Fe, Ru, and Os). Adsorption energy calculations revealed that NO undergoes physical adsorption on pristine g-C_3N_4 but chemical adsorption on TM-embedded g-C_3N_4. TM incorporation significantly enhanced NO adsorption, with the adsorption energy for Os-embedded g-C_3N_4 reaching −3.14 eV, compared to only −0.54 eV for pristine g-C_3N_4. Löwdin charge analysis indicated that in all TM-embedded configurations, electrons are transferred from

the d orbitals of the TM atoms to the π* orbitals of NO molecules, facilitating their activation. Among them, Os-embedded g-C_3N_4 exhibited superior characteristics for both sensing and removing environmental NO gas.

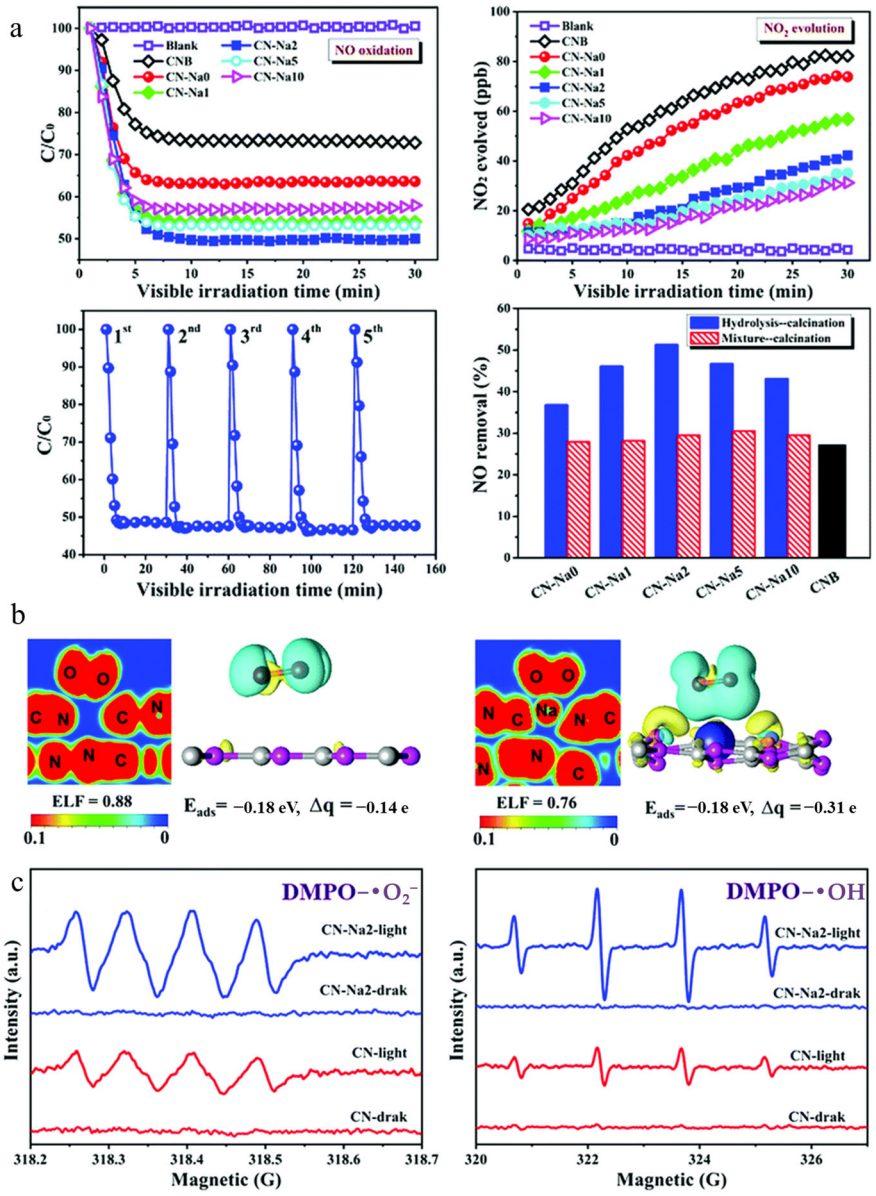

Figure 4. The photocatalytic NO oxidation performance (**a**), electronic local function and the charge difference distribution (**b**) of pristine g-C_3N_4 and Na-doped g-C_3N_4; and the ESR spectra for DMPO-•O_2^- and DMPO-•OH (**c**). [45] Copyright 2020, Royal Society of Chemistry.

3.2.3. Multi-Element Doping

Multi-element doping or co-intercalation is an effective strategy to further enhance the electronic structure and photocatalytic performance of g-C_3N_4. By leveraging the synergistic effects of different elements, issues such as low charge separation efficiency and insufficient active sites can be effectively addressed.

For instance, the intercalation of K^+ and Cl^- ions into the g-C_3N_4 interlayers can serve as efficient channels for electron and hole transport, respectively. This effectively separates charge carriers and significantly enhances the photocatalytic NO oxidation activity of g-C_3N_4 [52]. In amorphous g-C_3N_4, O and Ba can function as surface electron capture regulators and interlayer electron capture media, respectively. They promote

the convergence and localization of delocalized electrons within the g-C_3N_4 layers. This modified internal electronic structure favors the adsorption and activation of NO and O_2, prolongs the lifetime of photogenerated carriers, accelerates spatial charge separation, significantly enhances the generation of reactive oxygen species, and simultaneously inhibits the formation of toxic NO_2 [53].

Co-doping of O and La into g-C_3N_4 can be achieved via co-pyrolysis of $La_2(CO_3)_3$ and urea [54]. The strong electronegativity of surface O atoms leads to electron localization, activating NO to form NO^+ intermediates. This process also significantly promotes the generation of $\bullet O_2^-$ and •OH radicals from O_2, accelerating the conversion of NO to nitrate. Concurrently, incorporating La into g-C_3N_4 establishes directional electron transport channels between layers, enhancing carrier separation efficiency and overall photocatalytic performance.

The intercalation of Na^+ and Li^+ ions can expand the interlayer spacing of g-C_3N_4, facilitating the diffusion, adsorption, and activation of NO within the galleries. This process also reduces the probability of photogenerated charge recombination, leading to higher yields of reactive oxygen species and lowering the energy barrier for the oxidation of NO_2 to NO_3^-. Consequently, after 30 min of visible light irradiation, Na and Li co-doped g-C_3N_4 achieved a high NO removal rate of 81.1% [55].

3.3. Defect Engineering

Introducing defects into g-C_3N_4 is a highly effective strategy for enhancing its photocatalytic performance [58]. Defects can function as active sites, modulating the adsorption and activation of NO and O_2. Furthermore, defect states formed within the band gap can extend the light absorption range and promote the separation of photogenerated charge carriers. Common defects include carbon (C) vacancies and nitrogen (N) vacancies, which correspond to missing atomic sites within the g-C_3N_4 lattice. Different types of vacancies can distinctly influence the band structure, active sites, and charge migration in g-C_3N_4, ultimately leading to different photocatalytic pathways and efficiencies for NO removal. Table 2 summa rises the current developments in g-C_3N_4-based photocatalysts with different defects for the photocatalytic oxidation of NO.

Table 2. Summary of g-C_3N_4-based photocatalysts with different defects for the photocatalytic oxidation of NO.

Materials	Light Source	NO	Removal Rate	Reaction Time (min)	Ref.
g-C_3N_4 nanotube with C vacancy	visible LED lamp ($\lambda \geq 448$ nm)	600 ppb	47.7%	30	[59]
H_2-treated g-C_3N_4 with N defect	150 W tungsten halogen lamp ($\lambda > 420$ nm)	600 ppb	30.4%	30	[60]
mesoporous N-deficient g-C_3N_4	Two 12 W visible LED lamp	550 ppm	60.61%	30	[61]
N_{2C}-deficient g-C_3N_4	300 W Xe arc lamp	400 ppb	32.8%	30	[62]
defect-rich borate-modified g-C_3N_4	300 W halogen lamp (λ: 420–700 nm)	500 ppb	44.1%	30	[63]
$N_{(ligancy-3)}$-vacancy-rich g-C_3N_4	30 W visible LED lamp	600 ppb	66.7%	40	[64]
N_{3C} vacancy g-C_3N_4	LED lamp ($\lambda \geq 420$ nm)	600 ppb	40.3%	60	[65]
g-C_3N_4 oxygen vacancies	300 W Xenon lamp ($\lambda > 420$ nm)	500 ppb	40.71%	25	[66]

Carbon vacancies have been shown to capture photoexcited electrons and transfer them to surface-adsorbed O_2 molecules. This process establishes an efficient electron transport pathway, thereby enhancing the adsorption and activation of O_2 on the g-C_3N_4 surface. As a result, more reactive oxygen species are generated, significantly improving the efficiency of NO oxidation [59].

Thermal treatment of g-C_3N_4 in a hydrogen atmosphere is an effective method for generating nitrogen (N) vacancies. Higher treatment temperatures lead to increased concentrations of N vacancies. These vacancies not only narrow the band gap of the resulting material (CN-H_x), enhancing its visible-light absorption, but also facilitate the separation and migration of photogenerated carriers, leading to progressively improved NO oxidation performance [60]. DFT calculations indicate that N vacancies located at N_2C sites are particularly favorable for the adsorption and activation of NO. The electron-rich environments created by these N vacancies promote stronger electron transfer between the catalyst surface and reactants. This interaction limits the formation of NO^+ intermediates while increasing the generation of reactive oxygen species, thereby favoring the conversion of NO into nitro compounds via reactive oxygen species and reducing the production of NO_2.

From the perspective of increasing specific surface area, maximizing active site availability, and promoting effective carrier separation, combining mesoporous structures with defect engineering is crucial for enhancing the photocatalytic activity of g-C_3N_4. For instance, the construction of mesoporous nitrogen-deficient carbon nitride (nmpg-C_3N_4) via a silica templating method resulted in a 25.1% enhancement in photocatalytic activity compared to bulk g-C_3N_4 [61]. The mesoporous structure not only exposes more active sites but also, due to quantum confinement effects, widens the band gap, thereby augmenting its redox capability. The nitrogen vacancies act as catalytic active sites and facilitate efficient separation of photogenerated carriers. Under the synergistic effect of the mesoporous architecture and defect engineering, nmpg-C_3N_4 generates increased amounts of $\bullet O_2^-$ and •OH radicals, enabling effective removal of ppb-level NO from air.

Wang et al. [62] employed an in situ soft chemical method to controllably prepare microtubular g-C_3N_4 with tunable concentrations of nitrogen vacancies (N_2C-deficient g-C_3N_4, Figure 5). The surface nitrogen vacancies not only enhance the material's adsorption capacity for O_2 and NO but also facilitate the dissociation and activation of O_2 molecules, lowering the energy barrier for $\bullet O_2^-$ formation. Additionally, the porous microtubular structure promotes reactant diffusion and directional charge carrier migration.

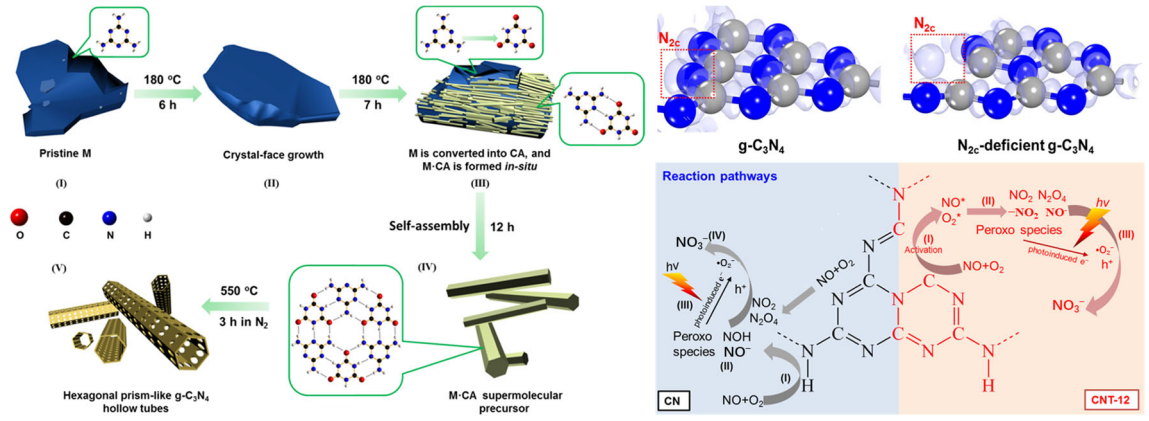

Figure 5. Schematic Representation of the Morphological Evolution of microtubular g-C_3N_4 with tunable nitrogen vacancies, calculated electron density difference diagrams of g-C_3N_4 and N_{2C}-deficient g-C_3N_4, and the proposed reaction pathways for adsorption and the photocatalytic oxidation of NO over pristine and N_{2C}-deficient g-C_3N_4 [62]. Copyright 2019, American Chemical Society.

Dual modification of g-C_3N_4, involving the introduction of both nitrogen vacancies and borate groups, can be achieved by immersing g-C_3N_4 in an aqueous $NaBH_4$ solution [63]. $NaBH_4$, with its high reduction potential, etches nitrogen atoms from the g-C_3N_4 framework, while its oxidation products (Na_3BO_3 and H_3BO_3) adsorb onto the surface, facilitating modification with BO_3^{3-} groups. The concentration of $NaBH_4$ allows for easy

adjustment of both nitrogen vacancy and borate group content. The resulting defect-rich borate-modified g-C_3N_4 efficiently removes ppb-level NO under visible light, with the removal efficiency showing a volcano-shaped trend relative to $NaBH_4$ concentration. The synergy between nitrogen vacancies and borate modifications enhances light absorption, carrier separation, and O_2 adsorption, thereby improving oxygen reduction and water oxidation reactions. This leads to increased generation of $\bullet O_2^-$ and •OH radicals, ultimately boosting NO removal performance. The relative contributions of nitrogen vacancies and borate groups to this synergy depend on the $NaBH_4$ concentration, with borate groups generally playing a predominant role. In situ DRIFTS studies confirm the complete conversion of NO to nitrate.

Nitrogen vacancies not only introduce impurity levels that reduce the band gap and shorten the charge migration path in g-C_3N_4 [64] but also serve as additional adsorption sites that promote the adsorption and activation of NO. They lower the activation energy for the conversion of NO_2 to NO_3^- and facilitate the activation of O_2 to generate $^1O_2$, thereby enhancing the oxidative capacity for NO while suppressing NO_2 formation [65].

In a specific study, Zhang et al. [66] synthesized a novel g-C_3N_4 material containing non-intrinsic oxygen vacancies (V_O-CN) using oxygen pre-doping and elimination techniques (Figure 6). Compared to pure g-C_3N_4, V_O-CN exhibited significantly enhanced photocatalytic activity under visible light, achieving a 54.3% higher NO removal rate with high selectivity towards NO_3^-. DFT calculations revealed that V_O-CN possesses a surface structure more favorable for the adsorption of O_2 and NO, and promotes O_2 activation by modulating local electron conduction. This enhances the generation of $\bullet O_2^-$ and •OH radicals from O_2, accelerating the oxidation of surface-adsorbed NO. Moreover, the oxygen vacancies in V_O-CN lead to the formation of intermediate bandgap states near the conduction band, which reduces the energy barrier for photogenerated electron transitions, promotes ground-state electron excitation, and suppresses electron-hole recombination, collectively contributing to increased reactive oxygen species generation.

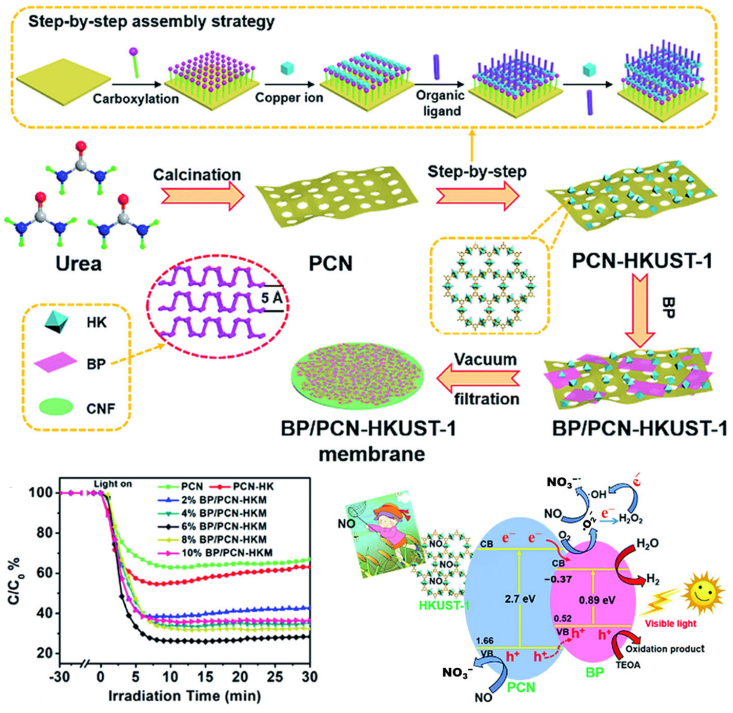

Figure 6. Schematic diagram of the preparation of BP/PCN-HKUST-1 membrane, its photocatalytic activity, and the proposed photocatalytic mechanism [67]. Copyright 2019, Royal Society of Chemistry.

3.4. Construction of Heterogeneous Structures

Heterojunctions can be categorized into several types, including Type-I, Type-II, S-scheme, Z-scheme, and Schottky junctions. By integrating two or more semiconductor materials with distinct band structures to form heterojunctions, it is possible to fully exploit the light absorption properties of each component. This strategy not only broadens the overall light absorption spectrum but also enhances light harvesting efficiency. Moreover, the built-in electric field at the heterointerface promotes the directional migration of charge carriers while effectively suppressing the recombination of photogenerated electron-hole pairs. Interactions between different materials can also modulate the chemical microenvironment at the interface, potentially enhancing reactant adsorption/activation and inhibiting competitive side reactions. Combining heterojunction construction with other strategies, such as morphology control, defect engineering, and elemental doping, can further optimize the NO removal performance of g-C_3N_4-based composites by synergistically improving light capture, charge separation, and surface reaction kinetics [19]. Table 3 lists the CN-based heterojunctions used for photocatalytic removal of NO. The specific progress of each type of material will be introduced in detail later.

Table 3. Summary of g-C_3N_4-based heterojunctions for photocatalytic removal of NO.

Materials	Heterojunction Type	Light Source	NO	Removal Rate	Reaction Time (min)	Ref.
BP/porous g-C_3N_4-HKUST-1	Type-I	Two 300 W Xenon lamp	600 ppb	74%	30	[67]
Mo-g-C_3N_4/g-C_3N_4	Type-I	150 W metal halide lamp (λ > 420 nm)	500 ppb	36%	30	[68]
0D-2D $AgVO_3$/g-C_3N_4	Type-II	300 W xenon lamp	600 ppb	65%	30	[69]
oxygen vacancy Bi_2WO_6/g-C_3N_4	Type-II	250 W Xe lamp	500 ppb	61.2%	30	[70]
g-C_3N_4/$BiVO_4$	Type-II	350 W Xe lamp	400 ppb	50%	360	[71]
$BaWO_4$/g-C_3N_4	Type-II	Two 12 W LED lamp	520 ppb	42.17%	30	[72]
g-C_3N_4/TiO_2	Type-II	150 W tungsten lamps (λ < 400 nm)	550 ppb	65%	60	[73]
g-C_3N_4/P25	Type-II	500 W Xenon arc lamp (λ: 420–700 nm)	400 ppb	44%	30	[74]
Pd_1/g-C_3N_4-UiO-66-NH_2	Type-II	300 W Xenon lamp (λ > 380 nm)	40–70 ppb	93.91%	-	[75]
g-C_3N_4/NH_2-UiO-66/rGO	Type-II	300 W Xenon lamp (λ > 400 nm)	600 ppb	56.8%	60	[76]
Protonated g-C_3N_4/GO aerogel	Type-II	150 W metal halide lamp (λ > 420 nm)	500 ppb	46.1%	30	[77]
N-doped TiO_2/g-C_3N_4	Type-II	Incandescent lamps	600 ppb	46.1%	30	[78]
g-C_3N_4/Co_3O_4	Type-II	300 W Xenon lamp (λ > 420 nm)	600 ppb	57%	60	[79]
Nd_2O_3/tubular g-C_3N_4	Type-II	Two 12 W LED lamp	520 ppb	54.48%	30	[80]
1D/2D $BiPO_4$/g-C_3N_4	Type-II	300 W Xe lamp (λ > 420 nm)	400 ppb	46%	30	[81]
Ag_3PO_4/g-C_3N_4	Type-II	mercury lamp (λ > 290 nm)	-	51.09%	30	[82]
$Bi_2O_2CO_3$/g-C_3N_4	Type-II	300 W Xe arc lamp (λ > 420 nm)	400 ppb	34.8%	30	[83]
g-C_3N_4/$LaCO_3OH$	Type-II	300 W Xe arc lamp (λ > 420 nm)	400 ppb	30.3%	30	[84]
$FAPbBr_3$/g-C_3N_4	Type-II	Xenon lamp	-	58%	60	[85]
g-C_3N_4/Ag/Ag_3PO_4	Z-Scheme	300 W Xenon lamp (λ > 420 nm)	400 ppm	74%	90	[86]
g-C_3N_4/Au/$ZnIn_2S_4$	Z-Scheme	300 W Xenon lamp (λ > 420 nm)	600 ppb	59.7%	60	[87]

Table 3. *Cont.*

Materials	Heterojunction Type	Light Source	NO	Removal Rate	Reaction Time (min)	Ref.
g-C_3N_4@Ag/BiVO4	Z-Scheme	350 W Xenon lamp (λ > 420 nm)	400 ppb	83%	150	[88]
NVs-g-C_3N_4/Bi/$BiO_{1-x}I$	Z-Scheme	300 W Xenon lamp (λ > 420 nm)	600 ppb	71.3%	18	[89]
MXene-derived TiO_2@C/g-C_3N_4	Z-Scheme	500 W Xenon lamp (λ > 420 nm)	100 ppm	17.8% 94.0% (with H_2O_2)	50	[90]
g-$C_3N_{4(QDs)}$/GO-$InVO_4$ aerogel	Z-Scheme	300 W Xenon lamp (λ > 420 nm)	600 ppb	65%	30	[91]
g-C_3N_4/rGO/C-TiO_2	Z-Scheme	2 mW LED lamp (627 nm)	1 ppm	28%	-	[92]
PI/GO/g-C_3N_4	Z-Scheme	300 W Xenon lamp (λ > 420 nm)	600 ppb	46%	30	[93]
$NaLa(WO_4)_2$/g-C_3N_4	Z-Scheme	Two 12 W LED lamp	550 ppb	47.18%	30	[94]
SnS_2/g-C_3N_4	Z-Scheme	-	-	66.8%	20	[95]
$TiO_{2-x}N_y$/g-C_3N_4	Z-Scheme	Simulated solar light (λ > 410 nm)		60%	20	[96]
rTiO_2/g-$C_3N_{4\,QDs}$	Z-Scheme	500 W Xenon lamp (λ > 420 nm)	600 ppb	37.4%	30	[97]
TiO_2/C_3N_5	Z-Scheme	300 W Xenon lamp (λ > 420 nm)	450 ppb	67.1%	20	[98]
honeycomb-like g-C_3N_4	Z-Scheme	Xenon lamp (λ > 420 nm)	600 ppb	68%	30	[99]
Bi_2O_3/g-C_3N_4	S-Scheme	300 W solar light lamp	500 ppb	39.1%	30	[100]
SnO2/g-C_3N_4	S-Scheme	300 W Xenon lamp (λ > 420 nm)	500 ppb	35%	30	[101]
Pd/TiO_2@g-C_3N_4	S-Scheme	300 W Xenon lamp (λ > 420 nm)	500 ppb	77.1%	30	[102]
Sb_2WO_6/g-C_3N_4	S-Scheme	Xenon lamp (λ > 420 nm)	400 ppb	68%	30	[103]
S-TiO_2/g-C_3N_4	S-Scheme	white fluorescent lamps (with UV cut-off filter)	1 ppm	25.25%	60	[104]
Au/g-C_3N_4	Schottky junction	150 W tungsten halogen lamp (λ > 420 nm)	500 ppb	41.0%	30	[105]
Pd^0/g-C_3N_4	Schottky junction	300 W Xenon lamp (λ > 420 nm)	600 ppb	75%	9	[106]
Bi/g-C_3N_4	Schottky junction	150 W tungsten halogen lamp (λ > 420 nm)	500 ppb	60.8%	30	[107]

3.4.1. Type-I Heterojunction

In a Type-I heterojunction, both the conduction band (CB) and valence band (VB) of one semiconductor are encompassed within the band structure of the other. Based solely on band alignment, photogenerated carriers tend to migrate and accumulate in the semiconductor with the narrower band gap, which can promote carrier recombination. Thus, Type-I heterojunctions are generally considered less favorable for enhancing photocatalytic activity. However, some studies indicate that when semiconductors with different Fermi levels form a Type-I junction, an internal electric field (IEF) can be generated at the interface, potentially facilitating carrier separation [108].

For instance, Hu et al. [67] used porous g-C_3N_4 (PCN) as a support to incorporate the NO-adsorptive metal–organic framework HKUST-1, and further combined it with black phosphorus (BP) nanosheets to construct a ternary composite (Figure 6). This composite achieved a NO removal rate of 74%, significantly higher than that of pure PCN (36%) or the PCN/HKUST-1 binary composite (45%). The authors proposed that the Type-I heterojunction formed between BP and PCN/HKUST-1 effectively promoted the separation of photogenerated charges. In this system, BP accepted electrons and facilitated the reduction

of O_2 to $\bullet O_2^-$, while HKUST-1 increased the local NO concentration, thereby accelerating the NO oxidation process.

In another study, Zhang et al. [68] employed urea as a precursor to synthesize g-C_3N_4 in situ on amorphous Mo-doped g-C_3N_4, successfully fabricating a Mo-g-C_3N_4/g-C_3N_4 homojunction. The amorphous Mo-g-C_3N_4 acted as a template for g-C_3N_4 growth, leading to the formation of a Type-I heterojunction. Within this structure, electrons from the CB and holes from the VB of g-C_3N_4 migrated to the corresponding bands of Mo-g-C_3N_4. The strong interaction between the two materials broadened the visible-light response and facilitated the separation of photogenerated carriers. Furthermore, Mo atoms served as active sites, donating electrons to adsorbed O_2 to promote the generation of $\bullet O_2^-$, which subsequently oxidized NO to NO_2 and nitrate.

3.4.2. Type-II Heterojunction

In a Type-II heterojunction, the band structures of the two semiconductors are staggered. The difference in their chemical potentials causes band bending at the interface, generating an internal electric field. Driven by this field, photogenerated electrons transfer from the semiconductor with a higher CB to the one with a lower CB, while holes migrate in the opposite direction. This spatial separation of electrons and holes onto different components significantly enhances charge separation efficiency.

Liu et al. [69] synthesized a three-dimensional $AgVO_3$/g-C_3N_4/graphene hybrid aerogel via a two-step process (Figure 7). A Type-II heterojunction formed between zero-dimensional $AgVO_3$ and two-dimensional g-C_3N_4, effectively separating photogenerated electrons and holes. The g-C_3N_4 nanosheets were closely integrated with reduced graphene oxide (rGO) layers through electrostatic interactions, π-π stacking, and hydrogen bonding. The high conductivity of graphene accelerated charge transfer, while the 3D sponge-like aerogel structure enhanced light harvesting and NO adsorption capacity, collectively boosting the photocatalytic efficiency. This catalyst achieved 65% NO degradation with good recyclability, where $\bullet O_2^-$ and •OH were identified as the key active species.

Cheng et al. [70] developed a 2D-0D g-C_3N_4/Bi_2WO_6-OV (CN/BWO-OV) composite by integrating g-C_3N_4 nanosheets with oxygen-vacancy-rich Bi_2WO_6 quantum dots. The presence of Bi_2WO_6-OV enhanced light absorption and carrier generation. The synergistic effect of the Type-II heterojunction and oxygen vacancies improved electron-hole separation efficiency and extended carrier lifetime. The composite exhibited a high NO removal efficiency of 61.2% for low-concentration NO (0.5 ppm), substantially outperforming pure g-C_3N_4 and Bi_2WO_6-OV. Similarly, other Type-II heterojunctions like $BiVO_4$/g-C_3N_4 [71] and $BaWO_4$/g-C_3N_4 [72] have also demonstrated superior NO removal efficiencies compared to pure g-C_3N_4 under visible light irradiation.

A 3D foam composed of g-C_3N_4 and TiO_2 quantum dots showed over 65% NO removal and remarkable stability for indoor NO gas under visible light [73]. The porous foam structure provided a large specific surface area and continuous channels, facilitating light absorption and reactant diffusion. The embedded g-C_3N_4/TiO_2 Type-II heterojunction promoted carrier separation, yielding high quantum efficiency. In situ FTIR analysis indicated that NO was preferentially oxidized to NO^+, effectively suppressing NO_2 by-product formation. In a similar vein, embedding TiO_2 nanoparticles (P25) into the g-C_3N_4 layered structure via co-calcination with melamine created an intimately contacted g-C_3N_4-TiO_2 Type-II heterojunction [74]. This close interfacial contact more effectively inhibited charge recombination compared to mechanically mixed samples, leading to increased $\bullet O_2^-$ generation and higher NO removal efficiency.

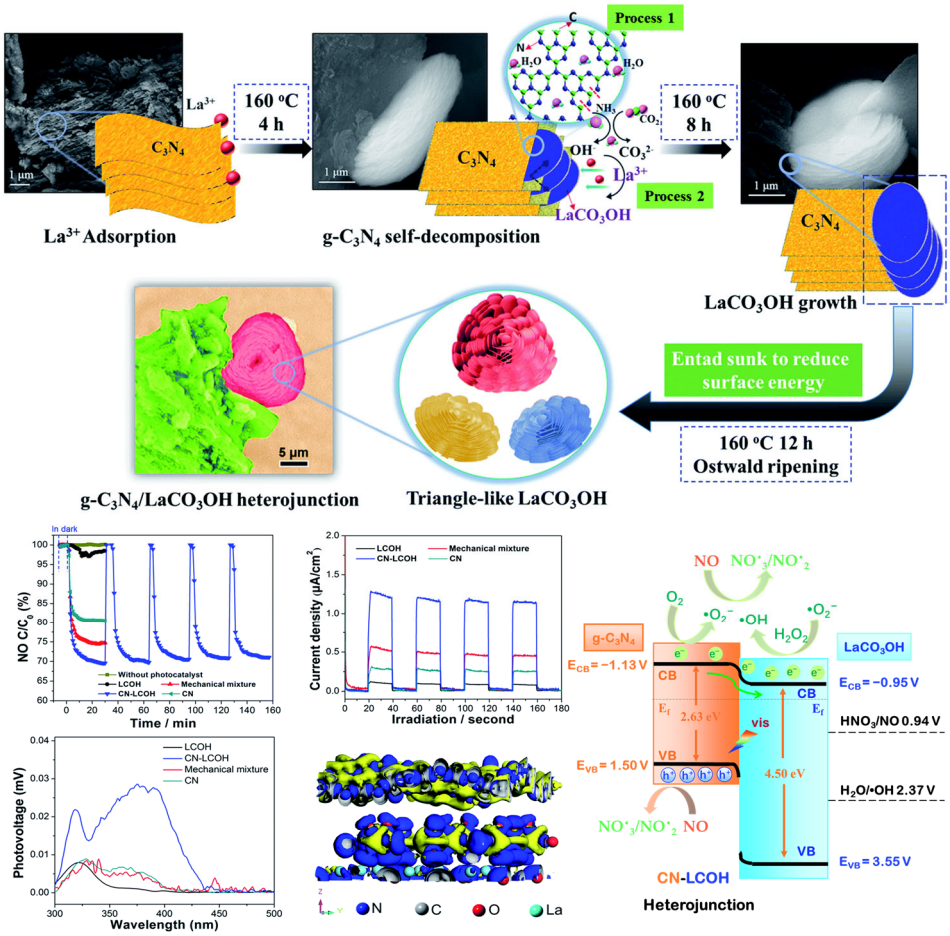

Figure 7. Schematic illustration of the synthesis process of g-C_3N_4/$LaCO_3OH$ heterojunctions (CN-LCOH), photoelectrochemical properties of the as-prepared photocatalysts, and the proposed photocatalytic mechanism of g-C_3N_4/$LaCO_3OH$ heterojunctions for NO degradation [84]. Copyright 2017, Royal Society of Chemistry.

Liu et al. [75] synthesized a photocatalytic-adsorption heterojunction by grinding Pd single-atom-anchored g-C_3N_4 and a Zr-based MOF (UiO-66-NH_2) for NO removal from actual coal-burning stove flue gas. Under visible light, the composite achieved 93.91% NO removal with only 2.73% NO_2 emission and negligible catalyst deactivation. DFT calculations revealed that Pd/g-C_3N_4 served as the active component for NO oxidation, while UiO-66-NH_2 effectively captured NO_2, suppressed its emission, and regenerated active sites. The internal electric field in the Type-II Pd/g-C_3N_4/UiO-66-NH_2 heterojunction significantly enhanced carrier separation and transfer. Using rGO aerogel as a support for g-C_3N_4/UiO-66-NH_2 further leveraged the activity of the Type-II heterojunction and provided additional charge transfer pathways [76].

Protonation can reverse the surface charge of g-C_3N_4 from negative to positive, enabling it to couple with negatively charged graphene oxide (GO) nanosheets via strong electrostatic self-assembly, which accelerates carrier transfer [77]. The GO aerogel support offers a rich porous structure and large specific surface area, enhancing NO adsorption. The blackbody effect and surface functional groups on GO improve visible light absorption, while its high conductivity facilitates electron-hole separation. Introducing hydrogen atoms onto the nitrogen atoms of g-C_3N_4 promotes oxygen activation, aiding the oxidation of NO and NO_2 to nitrate. The protonated g-C_3N_4/GO Type-II heterojunction inhibits charge recombination, resulting in a NO removal rate of 46.1% with a low NO_2 generation rate of 2.4%.

Other semiconductors, including TiN-derived N-doped TiO_2 [78], Co_3O_4 [79], Nd_2O_3 [80], $BiPO_4$ [81], Ag_3PO_4 [82], $Bi_2O_2CO_3$ [83], $LaCO_3OH$ [84] and formamidinium lead bromide ($FAPbBr_3$) [85] can also form Type-II heterojunctions with g-C_3N_4. These composites have been demonstrated to enhance carrier separation efficiency and improve the photocatalytic oxidation of NO.

3.4.3. Z-Scheme Heterojunction

While Type-II heterojunctions promote carrier separation, the migration of electrons to a lower-potential CB and holes to a lower-potential VB can thermodynamically reduce the overall redox capability. Kinetically, the repulsive force between electrons and electrons (holes and holes) impedes charge carrier transfer. In contrast, Z-Scheme heterojunctions utilize an internal conductive medium or an internal electric field to facilitate the recombination of less useful charge carriers (electrons in the lower-CB with holes in the higher-VB). This mechanism retains electrons with strong reducing power in the higher CB and holes with strong oxidizing power in the lower VB, thereby maximizing redox performance while achieving effective charge separation [109].

A ternary Z-Scheme g-C_3N_4/Ag/Ag_3PO_4 (AP-CN) heterojunction removed 74% of NO within 90 min under visible light, which is 3.5 and 1.8 times more effective than g-C_3N_4 and Ag_3PO_4 alone, respectively [86]. In this system, Ag nanoparticles acted as an electron mediator, enabling electrons from the CB of Ag_3PO_4 to recombine with holes in the VB of g-C_3N_4. This process retained highly reducing electrons in the CB of g-C_3N_4 and highly oxidizing holes in the VB of Ag_3PO_4. The Z-Scheme mechanism facilitated charge separation, prolonged carrier lifetime, and promoted the generation of $\bullet O_2^-$ and •OH radicals, which synergistically oxidized NO to NO_3^-. Increased surface area, improved hydrophilicity, and enhanced visible light capture also contributed to the activity. Similarly, an all-solid-state Z-Scheme g-C_3N_4/Au/$ZnIn_2S_4$ heterojunction, with Au as the electron mediator, also exhibited excellent NO oxidation activity [87].

Beyond noble metals, Bi metal also exhibits a surface plasmon resonance (SPR) effect. Under light irradiation, these metals can generate high-energy hot carriers that participate in photocatalytic reactions, thereby enhancing the optical properties of the material system. Wang et al. [89] constructed a Z-Scheme NVs-g-C_3N_4/Bi/$BiO_{1-x}I$ heterojunction via an HNO_3-assisted in situ solvothermal method. In the strongly acidic environment, -NH_2 groups on g-C_3N_4 were detached, creating disordered micropores and nitrogen vacancies (NVs). Concurrently, in situ grown BiOI nanosheets underwent partial reduction of Bi^{3+} to Bi^0, and lattice oxygen escaped to form oxygen vacancies. The synergy of NVs, oxygen vacancies, disordered micropores, and SPR-active Bi enabled full-spectrum absorption. Interface polarization-induced band shifts resulted in a Z-Scheme alignment that enhanced redox capabilities. Defects and the local electromagnetic field from Bi synergistically improved charge separation efficiency and prolonged carrier lifetime. The composite demonstrated 71.30% NO removal under visible light while significantly inhibiting NO_2 generation.

Carbon materials can also serve as electron mediators. A one-step calcination of Ti_3AlC_2, fluorides, and melamine in CO_2 atmosphere simultaneously etched Ti_3AlC_2, generated g-C_3N_4, and oxidized Ti_3C_2 to TiO_2@C [90]. The resulting TiO_2@C/g-C_3N_4 composite achieved a 94.0% NO removal rate in a photo-Fenton system at room temperature, significantly outperforming pure photocatalytic or Fenton reactions. The Z-scheme heterojunction between TiO_2@C and g-C_3N_4 enhanced charge separation and effectively activated H_2O_2 to generate $\bullet O_2^-$ and •OH radicals for complete NO oxidation. Other systems like g-$C_3N_{4(QDs)}$/GO-$InVO_4$ [91], g-C_3N_4/rGO/C-TiO_2 [92] and perylene imide

(PI)/GO/g-C_3N_4 [93] also operate via Z-scheme mechanisms that extend carrier lifetime and enhance NO oxidation activity.

Z-scheme heterojunctions can also form through direct contact between two semiconductors without a mediator. The $NaLa(WO_4)_2$/g-C_3N_4 Z-scheme heterojunction efficiently separated carriers while maintaining high redox capacity, achieving a NO removal rate of 47.18%, which was 16.51% higher than pure g-C_3N_4 [94]. In situ DRIFTS showed that NO was first oxidized to NO_2 by •OH and $•O_2^-$, and then ultimately converted to nitrite/nitrate.

Wang et al. [95] synthesized SnS_2/g-C_3N_4 composites via a solvothermal method. Under high-throughput simulated flue gas, the composites achieved 66.8% NO removal with excellent five-cycle reusability. XPS and DFT calculations confirmed strong interfacial interactions and a Z-scheme charge transfer mechanism. ESR spectra indicated that the composite facilitated the generation of •OH and $•O_2^-$. In situ DRIFTS showed that SnS_2/g-C_3N_4 promoted the conversion of NO to nitrate via nitrite and cis-$N_2O_2^{2-}$ intermediates.

Nitrogen doping can narrow the bandgap of TiO_2 and induce a mixed rutile/anatase phase. The band structure differences between these phases create an internal heterojunction within TiO_2, while a Z-scheme heterojunction forms between TiO_2 and g-C_3N_4, collectively enhancing charge separation and transfer [96]. Compared to single-phase TiO_2/g-C_3N_4, the dual-phase TiO_2/g-C_3N_4 composite exhibited superior NO oxidation capability. Other TiO_2/carbon nitride-based Z-scheme heterojunctions include rutile-TiO_2/g-$C_3N_{4(QDs)}$ [97] and P25/C_3N_5 [98].

A honeycomb-like g-C_3N_4 heterojunction (Figure 8), synthesized by co-calcining thiourea and urea, achieved 68% removal of low-concentration NO (600 ppb) under visible light, outperforming g-C_3N_4 derived from a single precursor [99]. The unique honeycomb structure enhanced light absorption through multiple internal reflections. High interface compatibility and a Z-scheme charge transfer mechanism significantly promoted the separation and migration of photogenerated carriers.

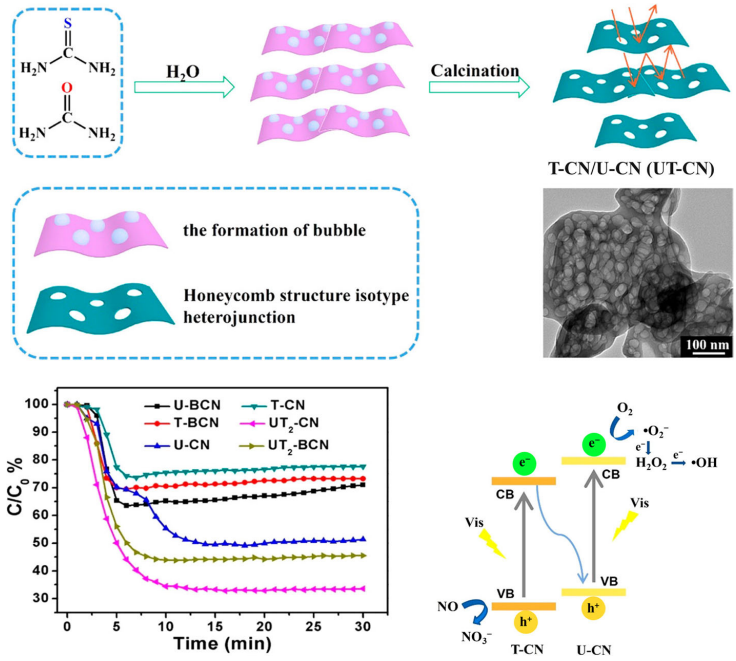

Figure 8. Schematic illustration of the fabrication of a honeycomb-like g-C_3N_4 heterojunction (T-CN/U-CN, UT-CN), visible-light photocatalytic activities of the g-C_3N_4 samples for removal of NO, and photocatalytic mechanism of NO removal by UT-CN samples under visible-light illumination [99]. Copyright 2018, Royal Society of Chemistry.

3.4.4. S-Scheme Heterojunction

Yu's research group [110] introduced a novel stepped (S-Scheme) heterojunction concept derived from the direct Z-Scheme heterojunction (Figure 9). The S-Scheme heterojunction comprises an oxidative photocatalyst (OP) and a reductive photocatalyst (RP). A fundamental requirement for the formation of a S-Scheme heterojunction is that both the conduction band position and Fermi level of RP must be higher than those of OP, with either RP or OP being capable of existing as n-type or p-type semiconductors. Upon contact between the two semiconductors, electrons will migrate from RP to OP at the interface due to the elevated Fermi level of RP, resulting in electron depletion in RP and consequently rendering it positively charged. In contrast, OP accepts these electrons and becomes negatively charged. This interaction leads to upward or downward band bending at the interface between RP and OP, establishing an internal electric field directed from RP towards OP. Under the combined influence of this internal electric field, Coulomb attraction, and band bending effects, photogenerated electrons are transferred from the conduction band (CB) of OP to the valence band (VB) of RP. Consequently, within this S-type photocatalytic system, electrons are retained in the CB of RP while holes accumulate in the VB of OP. This configuration demonstrates robust redox capabilities along with exceptional charge separation efficiency, thereby significantly enhancing photocatalytic performance [111].

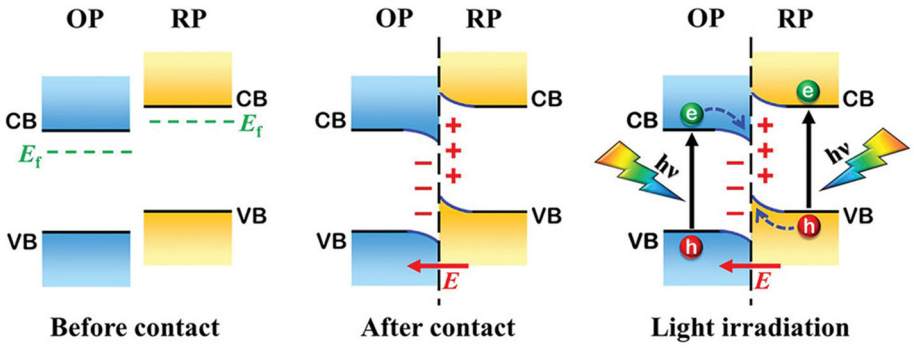

Figure 9. Charge-transfer processes in an S-Scheme heterojunction [110]. Copyright 2021, Wiley-VCH.

Tran et al. [100] developed an S-scheme Bi_2O_3/g-C_3N_4 heterojunction by modifying g-C_3N_4 with α-Bi_2O_3 micro-rods. It achieved a 39.1% NO removal under 30 min of visible light, 1.6 times higher than the individual components, and maintained over 35% removal after five cycles. Radical trapping experiments identified photogenerated holes as the primary active species. In another example, an S-scheme heterojunction between g-C_3N_4 and SnO_2 induced interface band bending, effectively separating charges and exhibiting strong oxidation capability [101]. It achieved 35% removal of 500 ppb NO with minimal NO_2 generation (~2%), whereas pure g-C_3N_4 produced up to 30% NO_2.

Pham et al. [102] synthesized Pd/TiO_2@g-C_3N_4 composites via wet impregnation. The NO removal efficiencies under sunlight and visible light were 77.1% and 67.2%, respectively. The SPR effect of Pd nanoparticles reduced the composite's band gap, enhancing visible light absorption. Photogenerated holes in TiO_2 played a major role in oxidation, while Pd nanoparticles acted as electron traps, promoting ROS generation and inhibiting charge recombination. The S-scheme heterojunction between TiO_2 and g-C_3N_4 effectively reduced recombination rates and provided active sites for redox reactions, promoting $\bullet O_2^-$ generation and achieving high NO oxidation efficiency.

An Sb_2WO_6/g-C_3N_4 composite with an S-scheme heterojunction demonstrated over 68% removal efficiency for continuously flowing NO (400 ppb) within 30 min under visible light [103]. Radical trapping experiments confirmed that $\bullet O_2^-$ and h^+ were the main active species. Transient photocurrent and PL spectra indicated enhanced charge separation.

DRIFTS analysis revealed that photocatalytic NO removal primarily proceeded via an oxygen-induced pathway.

Hossain et al. [104] synthesized an S-TiO_2/g-C_3N_4 heterojunction by co-pyrolyzing titanium-based flocculation dye sludge-derived TiO_2 (S-TiO_2) with melamine. Under UV light, 15.18% of atmospheric NO was removed within one hour. The enhanced activity was attributed to the narrowed band gap and reduced charge recombination rate.

3.4.5. Schottky Junction

A Schottky junction is formed at the interface between a metal and an n-type semiconductor, creating a Schottky barrier due to differences in their work functions. This configuration facilitates the effective separation of photogenerated carriers.

The surface plasmon resonance (SPR) effect of gold (Au) enhances light absorption in Au-loaded g-C_3N_4 [105]. Furthermore, Au promotes the adsorption and activation of NO and facilitates the generation of reactive oxygen species, improving NO removal efficiency. The Schottky junction in Au/g-C_3N_4 (Au@CN) significantly enhances electron transfer and charge separation, leading to increased NO removal rates while suppressing toxic NO_2 formation. DRIFTS and DFT calculations suggest that NO can be directly converted to nitrate at the active sites. In another study, Pd nanoparticles (Pd^0) were anchored onto nitrogen vacancies in g-C_3N_4 via coordination bonds between N atoms and Pd^{2+} ions [106]. The N vacancies adjacent to Pd^0 nanoparticles exhibited a thermal island effect, which synergistically reduced the competitive adsorption between NO and O_2 and promoted charge transfer, significantly enhancing photocatalytic NO removal activity.

Jiang et al. [107] used organic colloidal solutions to precisely control the size of Bi nanoparticles, thereby regulating the density of Bi/g-C_3N_4 heterojunctions and optimizing SPR intensity for photocatalytic NO oxidation. The study found that g-C_3N_4 modified with 12 nm Bi nanoparticles achieved a 60.8% NO removal rate for ppb-level NO in continuous flow, significantly outperforming g-C_3N_4 modified with smaller or larger Bi nanoparticles, as well as pure g-C_3N_4 (38.6%). On the catalyst surface, photogenerated holes, $\bullet O_2^-$, and •OH radicals all contributed to the oxidation of NO.

4. Conclusions and Prospect

Significant progress has been made in the research on g-C_3N_4-based photocatalytic NO removal, yet several challenges remain. The limited light absorption range, low separation efficiency of photogenerated carriers, and insufficient active sites continue to be fundamental constraints on photocatalytic performance. Addressing these issues requires comprehensive strategies spanning material design, structural modulation, and synthesis processes.

In terms of material design, defect engineering and heterostructure construction have been widely adopted to enhance the separation of electron-hole pairs and extend the range of visible light absorption. With regard to structural regulation, tailoring the morphology, size, and composition of g-C_3N_4 can effectively optimize its specific surface area and improve the distribution of active sites, thereby boosting photocatalytic efficiency. Constructing g-C_3N_4 with specific nanostructures further enhances light harvesting and charge transfer. Moreover, the rational design of active sites—such as introducing metal sites, defects, or dopants—is considered a crucial strategy for improving the efficacy of gas–solid photocatalytic NO_x removal.

In applied research, g-C_3N_4-based photocatalysis is gradually being extended to real-world environmental remediation scenarios, including flue gas denitrification, vehicle exhaust purification, and wastewater treatment. Research efforts are increasingly focused

not only on enhancing catalytic performance but also on ensuring long-term stability and poison resistance under complex environmental conditions.

From a synthesis perspective, developing green and environmentally friendly preparation methods has become a key focus. In terms of cost control, optimizing precursor selection, streamlining synthesis routes, and enabling material recycling show great potential for reducing the overall cost of g-C_3N_4-based photocatalysts, thereby facilitating their industrial adoption.

Despite these advances, the stability of g-C_3N_4-based catalysts under prolonged operation still requires improvement to meet the demands of practical applications. High preparation costs also remain a barrier to large-scale implementation, underscoring the need for continued research into cost-effective fabrication strategies.

Looking ahead, as material design and preparation technologies continue to advance, g-C_3N_4-based photocatalytic technology is expected to play an increasingly vital role in environmental governance, offering a sustainable pathway for nitrogen oxide pollution control.

Author Contributions: Writing—original draft preparation, X.N.; writing—review and editing, H.L.; conceptualization, F.C. and S.W. All authors have read and agreed to the published version of the manuscript.

Funding: The authors gratefully acknowledge the financial support of Open Project Program of State Key Laboratory of Low-carbon Smart Coal-fired Power Generation and Ultra-clean Emission (grant number: D2023FK081).

Data Availability Statement: No new data were created or analyzed in this study. Data sharing is not applicable to this article.

Conflicts of Interest: The authors declare that this study received funding from State Key Laboratory of Low-Carbon Smart Coal-Fired Power Generation and Ultra-Clean Emission, China Energy Science and Technology Research Institute Co., Ltd. The funder was not involved in the study design, collection, analysis, interpretation of data, the writing of this article or the decision to submit it for publication.

References

1. Wang, Y.; Tang, T.; Zhou, Q.; Xu, L.; Tang, C. Research progress in high-temperature SCR denitration: From catalyst innovations to reaction mechanism exploration. *Electr. Power Environ. Prot.* **2025**, *3*, 343–356. (In Chinese) [CrossRef]
2. Rezaei, F.; Rownaghi, A.A.; Monjezi, S.; Lively, R.P.; Jones, C.W. SO_x/NO_x Removal from Flue Gas Streams by Solid Adsorbents: A Review of Current Challenges and Future Directions. *Energy Fuels* **2015**, *29*, 5467–5486. [CrossRef]
3. Zhao, M.; Xue, P.; Liu, J.; Liao, J.; Guo, J. A review of removing SO_2 and NO_X by wet scrubbing. *Sustain. Energy Technol. Assess.* **2021**, *47*, 101451. [CrossRef]
4. Luo, C.; Ma, S.; Feng, Y.; Wang, C.; Zhao, G.; Feng, H.; Liu, J. Research status and development of flue gas denitrification technology in selective non-catalytic reduction. *Electr. Power Environ. Prot.* **2024**, *6*, 603–614. [CrossRef]
5. Alves, L.; Holz, L.I.V.; Fernandes, C.; Ribeirinha, P.; Mendes, D.; Fagg, D.P.; Mendes, A. A comprehensive review of NO_x and N_2O mitigation from industrial streams. *Renew. Sust. Enery Rev.* **2022**, *155*, 111916. [CrossRef]
6. Islam, A.; Teo, S.H.; Ng, C.H.; Taufiq-Yap, Y.H.; Choong, S.Y.T.; Awual, M.R. Progress in recent sustainable materials for greenhouse gas (NO_x and SO_x) emission mitigation. *Prog. Mater Sci.* **2023**, *132*, 101033. [CrossRef]
7. Shang, H.; Jia, H.; Li, P.; Li, H.; Zhang, W.; Li, S.; Wang, Q.; Xiao, S.; Wang, D.; Li, G.; et al. Highly selective and efficient photocatalytic NO removal: Charge carrier kinetics and interface molecular process. *Nano Res.* **2024**, *17*, 1003–1026. [CrossRef]
8. Nguyen, V.-H.; Nguyen, B.-S.; Huang, C.-W.; Le, T.-T.; Nguyen, C.C.; Le, T.T.N.; Heo, D.; Ly, Q.V.; Trinh, Q.T.; Shokouhimehr, M.; et al. Photocatalytic NO_x abatement: Recent advances and emerging trends in the development of photocatalysts. *J. Clean. Prod.* **2020**, *270*, 121912. [CrossRef]
9. Xue, T.; Li, J.; Chen, L.; Li, K.; Hua, Y.; Yang, Y.; Dong, F. Photocatalytic NO_x removal and recovery: Progress, challenges and future perspectives. *Chem. Sci.* **2024**, *15*, 9026–9046. [CrossRef] [PubMed]
10. Li, N.; Wang, C.; Zhang, K.; Lv, H.; Yuan, M.; Bahnemann, D.W. Progress and prospects of photocatalytic conversion of low-concentration NO_x. *Chin. J. Catal.* **2022**, *43*, 2363–2387. [CrossRef]

11. Pichat, P.; Herrmann, J.-M.; Courbon, H.; Disdier, J.; Mozzanega, M.-N. Photocatalytic oxidation of various compounds over TiO_2 and other semiconductor oxides; Mechanistic considerations. *Can. J. Chem. Eng.* **1982**, *60*, 27–32. [CrossRef]
12. Lu, X.; Wang, L.; Li, Z.; Wang, Z.; Gan, Y.; Hailili, R. 2D Bismuth-Based Nanomaterials for Photocatalytic Nitrogen Oxide Removal: Progress and Prospects. *ACS Sustain. Chem. Eng.* **2024**, *12*, 11444–11466. [CrossRef]
13. Ma, C.; Wei, J.; Jiang, K.; Chen, J.; Yang, Z.; Yang, X.; Yu, G.; Zhang, C.; Li, X. Typical layered structure bismuth-based photocatalysts for photocatalytic nitrogen oxides oxidation. *Sci. Total Environ.* **2023**, *855*, 158644. [CrossRef]
14. Ma, D.; Zhang, Z.; Zou, Y.; Chen, J.; Shi, J.-W. The progress of g-C_3N_4 in photocatalytic H_2 evolution: From fabrication to modification. *Coord. Chem. Rev.* **2024**, *500*, 215489. [CrossRef]
15. Zhou, M.; Ou, H.; Li, S.; Qin, X.; Fang, Y.; Lee, S.-C.; Wang, X.; Ho, W. Photocatalytic Air Purification Using Functional Polymeric Carbon Nitrides. *Adv. Sci.* **2021**, *8*, 2102376. [CrossRef]
16. Wang, Z.; Shi, X.; Chen, M.; Cao, J.; Ho, W.; Lee, S.; Wang, C.; Huang, Y. Polymeric carbon nitride-based photocatalysts for the removal of nitrogen oxides: A review. *Environ. Chem. Lett.* **2023**, *21*, 2913–2952. [CrossRef]
17. Wang, H.; Labidi, A.; Ren, M.; Shaik, F.; Wang, C. Recent progress of microstructure-regulated g-C_3N_4 in photocatalytic NO conversion: The pivotal roles of adsorption/activation sites. *Acta Phys. Chim. Sin.* **2025**, *41*, 100039. [CrossRef]
18. Lasek, J.; Yu, Y.-H.; Wu, J.C.S. Removal of NO_x by photocatalytic processes. *J. Photochem. Photobiol. C* **2013**, *14*, 29–52. [CrossRef]
19. Hailili, R.; Gan, Y. Tailoring Multiscale Interfaces in Heterojunction Photocatalysis for NO_x Removal. *ACS Appl. Mater. Interfaces* **2025**, *17*, 39809–39844. [CrossRef] [PubMed]
20. Yuan, R.; Wang, M.; Liao, L.; Hu, W.; Liu, Z.; Liu, Z.; Guo, L.; Li, K.; Cui, Y.; Lin, F.; et al. 100% N_2O inhibition in photocatalytic NO_x reduction by carbon particles over Bi_2WO_6/TiO_2 Z-scheme heterojunctions. *Chem. Eng. J.* **2023**, *453*, 139892. [CrossRef]
21. Cui, W.; Wang, J.; Li, Y.; Liu, P.; Dong, F. Photocatalytic NO removal: Complete oxidation and reduction reaction for by-product inhibition and end-product recovery. *Environ. Sci. Nano* **2025**, *12*, 67–97. [CrossRef]
22. Xiao, L.; Chen, P.; Yang, W.; Zhao, X.; Dong, F. Photocatalytic reaction mechanisms at the gas-solid interface for environmental and energy applications. *Catal. Sci. Technol.* **2021**, *11*, 7807–7839. [CrossRef]
23. Bari, G.A.K.M.R.; Islam, M.; Jeong, J.-H. Materials Design and Development of Photocatalytic NO_x Removal Technology. *Metals* **2024**, *14*, 423. [CrossRef]
24. Chen, R.; Wang, J.; Zhang, C.; Sun, Y.; Li, J.; Dong, F. Purification and Value-Added Conversion of NO_x under Ambient Conditions with Photo-/Electrocatalysis Technology. *Environ. Sci. Technol.* **2025**, *59*, 1013–1033. [CrossRef] [PubMed]
25. Shi, Y.; Yang, Z.; Shi, L.; Li, H.; Liu, X.; Zhang, X.; Cheng, J.; Liang, C.; Cao, S.; Guo, F.; et al. Surface Boronizing Can Weaken the Excitonic Effects of BiOBr Nanosheets for Efficient O_2 Activation and Selective NO Oxidation under Visible Light Irradiation. *Environ. Sci. Technol.* **2022**, *56*, 14478–14486. [CrossRef] [PubMed]
26. Liang, H.; Zhao, J.; Wang, A.; Kannan, P.; Jing, S.; Chen, F.; Tsiakaras, P. Synthesis of novel nanoflowers-like P, K co-doped graphitic carbon nitride for efficient H_2O_2 photoproduction. *J. Colloid Interface Sci.* **2025**, *677*, 729–739. [CrossRef]
27. Liang, H.; Wang, A.; Cheng, R.; Chen, F.; Kannan, P.; Molochas, C.; Tsiakaras, P. K co-doped graphitic phase carbon nitride for efficient photocatalytic H_2O_2 production. *Chem. Eng. J.* **2024**, *489*, 151145. [CrossRef]
28. Ai, W.; Wang, J.; Wen, J.; Wang, S.; Tan, W.; Zhang, Z.; Liang, K.; Zhang, R.; Li, W. Research landscape and hotspots of selective catalytic reduction (SCR) for NO_x removal: Insights from a comprehensive bibliometric analysis. *Environ. Sci. Pollut. Res.* **2023**, *30*, 65482–65499. [CrossRef]
29. Yuan, S.; Dai, L.; Xie, M.; Liu, J.; Peng, H. Modification optimization and application of graphitic carbon nitride in photocatalysis: Current progress and future prospects. *Chem. Eng. Sci.* **2024**, *296*, 120245. [CrossRef]
30. Wu, H.; Chen, D.; Li, N.; Xu, Q.; Li, H.; He, J.; Lu, J. Hollow porous carbon nitride immobilized on carbonized nanofibers for highly efficient visible light photocatalytic removal of NO. *Nanoscale* **2016**, *8*, 12066–12072. [CrossRef]
31. Sano, T.; Tsutsui, S.; Koike, K.; Hirakawa, T.; Teramoto, Y.; Negishi, N.; Takeuchi, K. Activation of graphitic carbon nitride (g-C_3N_4) by alkaline hydrothermal treatment for photocatalytic NO oxidation in gas phase. *J. Mater. Chem. A* **2013**, *1*, 6489–6496. [CrossRef]
32. Ma, H.; Jia, Y.; Zhu, G.; Zhang, F.; Rhee, S.; Lee, B.; Liu, C. Study of cyano and hydroxyl groups modification on the properties of porous carbon nitride synthesized by using a salt assistant method. *Appl. Surf. Sci.* **2020**, *507*, 144885. [CrossRef]
33. Wang, H.; Xu, X.; Labidi, A.; Ren, H.; Allam, A.A.; Rady, A.; Huang, Y.; Wei, S.; Padervand, M.; Ghasemi, S.; et al. Cyano/Hydroxyl Groups Co-Functionalized g-C_3N_4 for Photocatalytic NO Removal: A Synergistic Strategy towards Inhibition of Toxic Intermediate NO_2. *Catalysts* **2023**, *13*, 1433. [CrossRef]
34. Yi, J.; Liao, J.; Xia, K.; Song, Y.; Lian, J.; She, X.; Liu, Y.; Yuan, S.; Dong, F.; Xu, H.; et al. Integrating the merits of two-dimensional structure and heteroatom modification into semiconductor photocatalyst to boost NO removal. *Chem. Eng. J.* **2019**, *370*, 944–951. [CrossRef]
35. Fang, Z.; Zhou, M.; Lin, Z.; Yang, C.; Hou, Y.; Yu, J.C.; Zhang, J.; Wang, X. Amide bonded polymeric carbon nitride for photocatalytic O_2 activation and NO oxidation. *Appl. Catal. B* **2024**, *353*, 124022. [CrossRef]

36. Zhang, R.; Ma, M.; Zhang, Q.; Dong, F.; Zhou, Y. Multifunctional g-C_3N_4/graphene oxide wrapped sponge monoliths as highly efficient adsorbent and photocatalyst. *Appl. Catal. B* **2018**, *235*, 17–25. [CrossRef]
37. Cui, Y.; Huang, X.; Wang, T.; Jia, L.; Nie, Q.; Tan, Z.; Yu, H. Graphene quantum dots/carbon nitride heterojunction with enhanced visible-light driven photocatalysis of nitric oxide: An experimental and DFT study. *Carbon* **2022**, *191*, 502–514. [CrossRef]
38. Gu, Z.; Zhang, B.; Asakura, Y.; Tsukuda, S.; Kato, H.; Kakihana, M.; Yin, S. Alkali-assisted hydrothermal preparation of g-C_3N_4/rGO nanocomposites with highly enhanced photocatalytic NO_x removal activity. *Appl. Surf. Sci.* **2020**, *521*, 146213. [CrossRef]
39. Abdellatif, H.R.S.; Zhang, G.; Wang, X.; Xie, D.; Irvine, J.T.S.; Ni, J.; Ni, C. Boosting photocatalytic oxidation on graphitic carbon nitride for efficient photocatalysis by heterojunction with graphitic carbon units. *Chem. Eng. J.* **2019**, *370*, 875–884. [CrossRef]
40. Hou, S.; Gao, X.; Lv, X.; Zhao, Y.; Yin, X.; Liu, Y.; Fang, J.; Yu, X.; Ma, X.; Ma, T.; et al. Decade Milestone Advancement of Defect-Engineered g-C_3N_4 for Solar Catalytic Applications. *Nano-Micro Lett.* **2024**, *16*, 70. [CrossRef] [PubMed]
41. Ran, M.; Li, J.; Cui, W.; Li, Y.; Li, P.; Dong, F. Efficient and stable photocatalytic NO removal on C self-doped g-C_3N_4: Electronic structure and reaction mechanism. *Catal. Sci. Technol.* **2018**, *8*, 3387–3394. [CrossRef]
42. Wang, Z.; Chen, M.; Huang, Y.; Shi, X.; Zhang, Y.; Huang, T.; Cao, J.; Ho, W.; Lee, S.C. Self-assembly synthesis of boron-doped graphitic carbon nitride hollow tubes for enhanced photocatalytic NO_x removal under visible light. *Appl. Catal. B* **2018**, *239*, 352–361. [CrossRef]
43. Qi, Z.; Chen, J.; Zhou, W.; Li, Y.; Li, X.; Zhang, S.; Fan, J.; Lv, K. Synergistic effects of holey nanosheet and sulfur-doping on the photocatalytic activity of carbon nitride towards NO removal. *Chemosphere* **2023**, *316*, 137813. [CrossRef] [PubMed]
44. Luo, J.; Dong, G.; Zhu, Y.; Yang, Z.; Wang, C. Switching of semiconducting behavior from n-type to p-type induced high photocatalytic NO removal activity in g-C_3N_4. *Appl. Catal. B* **2017**, *214*, 46–56. [CrossRef]
45. Li, X.; Hu, Z.; Li, Q.; Lei, M.; Fan, J.; Carabineiro, S.A.C.; Liu, Y.; Lv, K. Three in one: Atomically dispersed Na boosting the photoreactivity of carbon nitride towards NO oxidation. *Chem. Commun.* **2020**, *56*, 14195–14198. [CrossRef] [PubMed]
46. Xiong, T.; Cen, W.; Zhang, Y.; Dong, F. Bridging the g-C_3N_4 Interlayers for Enhanced Photocatalysis. *ACS Catal.* **2016**, *6*, 2462–2472. [CrossRef]
47. Cui, W.; Li, J.; Cen, W.; Sun, Y.; Lee, S.C.; Dong, F. Steering the interlayer energy barrier and charge flow via bioriented transportation channels in g-C_3N_4: Enhanced photocatalysis and reaction mechanism. *J. Catal.* **2017**, *352*, 351–360. [CrossRef]
48. Li, J.; Cui, W.; Sun, Y.; Chu, Y.; Cen, W.; Dong, F. Directional electron delivery via a vertical channel between g-C_3N_4 layers promotes photocatalytic efficiency. *J. Mater. Chem. A* **2017**, *5*, 9358–9364. [CrossRef]
49. Zhou, M.; Dong, G.; Ma, J.; Dong, F.; Wang, C.; Sun, J. Photocatalytic removal of NO by intercalated carbon nitride: The effect of group IIA element ions. *Appl. Catal. B Environ.* **2020**, *273*, 119007. [CrossRef]
50. Zhou, M.; Dong, G.; Yu, F.; Huang, Y. The deep oxidation of NO was realized by Sr multi-site doped g-C_3N_4 via photocatalytic method. *Appl. Catal. B* **2019**, *256*, 117825. [CrossRef]
51. Zhang, R.; Cao, Y.; Doronkin, D.E.; Ma, M.; Dong, F.; Zhou, Y. Single-atom dispersed Zn-N_3 active sites bridging the interlayer of g-C_3N_4 to tune NO oxidation pathway for the inhibition of toxic by-product generation. *Chem. Eng. J.* **2023**, *454*, 140084. [CrossRef]
52. Xiong, T.; Wang, H.; Zhou, Y.; Sun, Y.; Cen, W.; Huang, H.; Zhang, Y.; Dong, F. KCl-mediated dual electronic channels in layered g-C_3N_4 for enhanced visible light photocatalytic NO removal. *Nanoscale* **2018**, *10*, 8066–8074. [CrossRef]
53. Cui, W.; Li, J.; Sun, Y.; Wang, H.; Jiang, G.; Lee, S.C.; Dong, F. Enhancing ROS generation and suppressing toxic intermediate production in photocatalytic NO oxidation on O/Ba co-functionalized amorphous carbon nitride. *Appl. Catal. B* **2018**, *237*, 938–946. [CrossRef]
54. Chen, P.; Wang, H.; Liu, H.; Ni, Z.; Li, J.; Zhou, Y.; Dong, F. Directional electron delivery and enhanced reactants activation enable efficient photocatalytic air purification on amorphous carbon nitride co-functionalized with O/La. *Appl. Catal. B* **2019**, *242*, 19–30. [CrossRef]
55. Zhou, M.; Zeng, L.; Li, R.; Yang, C.; Qin, X.; Ho, W.; Wang, X. Poly(heptazine imide) with Enlarged Interlayers Spacing for Efficient Photocatalytic NO Decomposition. *Appl. Catal. B* **2022**, *317*, 121719. [CrossRef]
56. Junaid, M.; Iqbal, M.; Ragab, A.H.; Al-Mhyawi, S.R.; Gumaah, N.F.; Jabbar, A.; Khan, I. Advanced theoretical insights into energetically favorable and structurally stable boron-doped graphitic carbon nitride for effective catalytic removal of nitrous oxide and carbon monoxide from industrial flue gases. *Environ. Sci. Pollut. Res.* **2025**, *32*, 14928–14943. [CrossRef]
57. Basharnavaz, H.; Habibi-Yangjeh, A.; Kamali, S.H. and Os—Embedded graphitic carbon nitride as a promising candidate for NO gas sensor: A first-principles investigation. *Mater. Chem. Phys.* **2019**, *231*, 264–271. [CrossRef]
58. Pundi, A.; Chang, C.-J. Synthesis, Characterization, and Roles of Vacancy Defects in Polymer and Graphitized Carbon Nitride Photocatalysts: A Comprehensive Review. *Polymers* **2025**, *17*, 334. [CrossRef]
59. Li, Y.; Gu, M.; Shi, T.; Cui, W.; Zhang, X.; Dong, F.; Cheng, J.; Fan, J.; Lv, K. Carbon vacancy in C_3N_4 nanotube: Electronic structure, photocatalysis mechanism and highly enhanced activity. *Appl. Catal. B* **2020**, *262*, 118281. [CrossRef]

60. Liao, J.; Cui, W.; Li, J.; Sheng, J.; Wang, H.; Dong, X.A.; Chen, P.; Jiang, G.; Wang, Z.; Dong, F. Nitrogen defect structure and NO^+ intermediate promoted photocatalytic NO removal on H_2 treated g-C_3N_4. *Chem. Eng. J.* **2020**, *379*, 122282. [CrossRef]
61. Lu, P.; Yang, Y.; Bai, J.; Zhao, Z.; Fu, M.; Hu, X.; He, Y. Defected mesoporous carbon nitride with quantum confinement effect for NO purification. *J. Alloys Compd.* **2023**, *934*, 167825. [CrossRef]
62. Wang, Z.; Huang, Y.; Chen, M.; Shi, X.; Zhang, Y.; Cao, J.; Ho, W.; Lee, S.C. Roles of N-Vacancies over Porous g-C_3N_4 Microtubes during Photocatalytic NO_x Removal. *ACS Appl. Mater. Interfaces* **2019**, *11*, 10651–10662. [CrossRef]
63. Cao, J.; Zhang, J.; Dong, X.A.; Fu, H.; Zhang, X.; Lv, X.; Li, Y.; Jiang, G. Defective borate-decorated polymer carbon nitride: Enhanced photocatalytic NO removal, synergy effect and reaction pathway. *Appl. Catal. B* **2019**, *249*, 266–274. [CrossRef]
64. Gu, W.; Lu, D.; Kondamareddy, K.K.; Li, J.; Cheng, P.; Ho, W.; Wang, Y.; Zhao, Z.; Wang, Z. Efficient photocatalytic decomposition of NO and mechanism insight enabled by $NaBH_4$-reduced $N_{(ligancy-3)}$-vacancy-rich-graphitic carbon nitride. *Mater. Today Phys.* **2024**, *46*, 101487. [CrossRef]
65. Li, Y.; Gu, M.; Zhang, M.; Zhang, X.; Lv, K.; Liu, Y.; Ho, W.; Dong, F. C_3N_4 with engineered three coordinated (N_3C) nitrogen vacancy boosts the production of $^1O_2$ for Efficient and stable NO photo-oxidation. *Chem. Eng. J.* **2020**, *389*, 124421. [CrossRef]
66. Zhang, C.; Xu, Y.; Bai, H.; Li, D.; Wei, L.; Feng, C.; Huang, Y.; Wang, Z.; Li, X.; Cui, X.; et al. Boosting visible-light photocatalytic NO removal by non-intrinsic oxygen vacancies in graphitic carbon nitride. *Nano Energy* **2024**, *121*, 109197. [CrossRef]
67. Hu, J.; Ji, Y.; Mo, Z.; Li, N.; Xu, Q.; Li, Y.; Xu, H.; Chen, D.; Lu, J. Engineering black phosphorus to porous g-C_3N_4-metal-organic framework membrane: A platform for highly boosting photocatalytic performance. *J. Mater. Chem. A* **2019**, *7*, 4408–4414. [CrossRef]
68. Zhang, R.; Zhang, A.; Cao, Y.; Wang, S.; Dong, F.; Zhou, Y. Mo-doped carbon nitride homojunction to promote oxygen activation for enhanced photocatalytic performance. *Chem. Eng. J.* **2020**, *401*, 126028. [CrossRef]
69. Liu, D.; Chen, D.; Li, N.; Xu, Q.; Li, H.; He, J.; Lu, J. Integration of 3D macroscopic graphene aerogel with 0D-2D $AgVO_3$-g-C_3N_4 heterojunction for highly efficient photocatalytic oxidation of nitric oxide. *Appl. Catal. B* **2019**, *243*, 576–584. [CrossRef]
70. Cheng, C.; Chen, D.; Li, N.; Li, H.; Xu, Q.; He, J.; Lu, J. Bi_2WO_6 quantum dots with oxygen vacancies combined with g-C_3N_4 for NO removal. *J. Colloid Interface Sci.* **2022**, *609*, 447–455. [CrossRef]
71. Ou, M.; Zhong, Q.; Zhang, S.; Yu, L. Ultrasound assisted synthesis of heterogeneous g-C_3N_4/$BiVO_4$ composites and their visible-light-induced photocatalytic oxidation of NO in gas phase. *J. Alloys Compd.* **2015**, *626*, 401–409. [CrossRef]
72. Wang, C.; Fu, M.; Cao, J.; Wu, X.; Hu, X.; Dong, F. $BaWO_4$/g-C_3N_4 heterostructure with excellent bifunctional photocatalytic performance. *Chem. Eng. J.* **2020**, *385*, 123833. [CrossRef]
73. Xiong, M.; Tao, Y.; Zhao, Z.; Zhu, Q.; Jin, X.; Zhang, S.; Chen, M.; Li, G. Porous g-C_3N_4/TiO_2 foam photocatalytic filter for treating NO indoor gas. *Environ. Sci. Nano* **2021**, *8*, 1571–1579. [CrossRef]
74. Ma, J.; Wang, C.; He, H. Enhanced photocatalytic oxidation of NO over g-C_3N_4-TiO_2 under UV and visible light. *Appl. Catal. B* **2016**, *184*, 28–34. [CrossRef]
75. Liu, J.; Huang, X.; Hu, L.; Liu, P.; Jia, L.; Sasaki, K.; Tan, Z.; Yu, H. Nitric oxide removal by synergistic photooxidation and adsorption using Pd_1/g-C_3N_4-UiO-66-NH_2 P-A heterojunction. *Chem. Eng. J.* **2023**, *476*, 146768. [CrossRef]
76. Zhou, Z.; Chen, D.; Li, N.; Xu, Q.; Li, H.; He, J.; Lu, J. Three-Dimensional g-C_3N_4/NH_2-UiO-66 graphitic aerogel hybrids with recyclable property for enhanced photocatalytic elimination of nitric oxide. *Chem. Eng. J.* **2021**, *418*, 129117. [CrossRef]
77. Zhang, R.; Zhang, A.; Yang, Y.; Cao, Y.; Dong, F.; Zhou, Y. Surface modification to control the secondary pollution of photocatalytic nitric oxide removal over monolithic protonated g-C_3N_4/graphene oxide aerogel. *J. Hazard. Mater.* **2020**, *397*, 122822. [CrossRef]
78. Jiang, G.; Cao, J.; Chen, M.; Zhang, X.; Dong, F. Photocatalytic NO oxidation on N-doped TiO_2/g-C_3N_4 heterojunction: Enhanced efficiency, mechanism and reaction pathway. *Appl. Surf. Sci.* **2018**, *458*, 77–85. [CrossRef]
79. Liu, D.; Chen, D.; Li, N.; Xu, Q.; Li, H.; He, J.; Lu, J. ZIF-67-Derived 3D Hollow Mesoporous Crystalline Co_3O_4 Wrapped by 2D g-C_3N_4 Nanosheets for Photocatalytic Removal of Nitric Oxide. *Small* **2019**, *15*, 1902291. [CrossRef]
80. Tan, Y.; Wei, S.; Liu, X.; Pan, B.; Liu, S.; Wu, J.; Fu, M.; Jia, Y.; He, Y. Neodymium oxide (Nd_2O_3) coupled tubular g-C3N4, an efficient dual-function catalyst for photocatalytic hydrogen production and NO removal. *Sci. Total Environ.* **2021**, *773*, 145583. [CrossRef]
81. Wang, X.; Ren, Y.; Li, Y.; Zhang, G. Fabrication of 1D/2D $BiPO_4$/g-C_3N_4 heterostructured photocatalyst with enhanced photocatalytic efficiency for NO removal. *Chemosphere* **2022**, *287*, 132098. [CrossRef] [PubMed]
82. Zhao, Z.; Fan, J.; Liu, W.; Xue, Y.; Yin, S. In-situ hydrothermal synthesis of Ag_3PO_4/g-C_3N_4 composite and their photocatalytic decomposition of NO_x. *J. Alloys Compd.* **2017**, *695*, 2812–2819. [CrossRef]
83. Wang, Z.; Huang, Y.; Ho, W.; Cao, J.; Shen, Z.; Lee, S.C. Fabrication of $Bi_2O_2CO_3$/g-C_3N_4 heterojunctions for efficiently photocatalytic NO in air removal: In-situ self-sacrificial synthesis, characterizations and mechanistic study. *Appl. Catal. B* **2016**, *199*, 123–133. [CrossRef]
84. Wang, Z.; Huang, Y.; Chen, L.; Chen, M.; Cao, J.; Ho, W.; Lee, S.C. In situ g-C_3N_4 self-sacrificial synthesis of a g-C_3N_4/$LaCO_3OH$ heterostructure with strong interfacial charge transfer and separation for photocatalytic NO removal. *J. Mater. Chem. A* **2018**, *6*, 972–981. [CrossRef]

85. Xie, B.; Chen, D.; Li, N.; Xu, Q.; Li, H.; He, J.; Lu, J. Fabrication of an $FAPbBr_3$/g-C_3N_4 heterojunction to enhance NO removal efficiency under visible-light irradiation. *Chem. Eng. J.* **2022**, *430*, 132968. [CrossRef]
86. Li, G.; Guo, J.; Hu, Y.; Wang, Y.; Wang, J.; Zhang, S.; Zhong, Q. Facile synthesis of the Z-scheme graphite-like carbon nitride/silver/silver phosphate nanocomposite for photocatalytic oxidative removal of nitric oxides under visible light. *J. Colloid Interface Sci.* **2021**, *588*, 110–121. [CrossRef]
87. Zhang, G.; Zhu, X.; Chen, D.; Li, N.; Xu, Q.; Li, H.; He, J.; Xu, H.; Lu, J. Hierarchical Z-scheme g-C_3N_4/Au/$ZnIn_2S_4$ photocatalyst for highly enhanced visible-light photocatalytic nitric oxide removal and carbon dioxide conversion. *Environ. Sci. Nano* **2020**, *7*, 676–687. [CrossRef]
88. Ou, M.; Wan, S.; Zhong, Q.; Zhang, S.; Song, Y.; Guo, L.; Cai, W.; Xu, Y. Hierarchical Z-scheme photocatalyst of g-C3N4@Ag/BiVO4 (040) with enhanced visible-light-induced photocatalytic oxidation performance. *Appl. Catal. B* **2018**, *221*, 97–107. [CrossRef]
89. Wang, M.; Xin, D.; Tan, G.; Qiu, Y.; Zhang, W.; Shi, M.; Shi, L. Defects and polarization charge cooperatively optimized Z-scheme NVs-g-C_3N_4/Bi/$BiO_{1-x}I$ heterojunction for full-spectrum catalytic organic pollutants mineralization and NO deep oxidation. *J. Alloys Compd.* **2025**, *1027*, 180651. [CrossRef]
90. Wang, T.; Yang, W.; Chang, L.; Wang, H.; Wu, H.; Cao, J.; Fan, H.; Wang, J.; Liu, H.; Hou, Y.; et al. One-step calcination synthesis of accordion-like MXene-derived TiO_2@C coupled with g-C_3N_4: Z-scheme heterojunction for enhanced photocatalytic NO removal. *Sep. Purif. Technol.* **2022**, *285*, 120329. [CrossRef]
91. Hu, J.; Chen, D.; Li, N.; Xu, Q.; Li, H.; He, J.; Lu, J. Fabrication of graphitic-C_3N_4 quantum dots/graphene-$InVO_4$ aerogel hybrids with enhanced photocatalytic NO removal under visible-light irradiation. *Appl. Catal. B* **2018**, *236*, 45–52. [CrossRef]
92. Noda, C.; Asakura, Y.; Shiraki, K.; Yamakata, A.; Yin, S. Synthesis of three-component C_3N_4/rGO/C-TiO_2 photocatalyst with enhanced visible-light responsive photocatalytic deNO_x activity. *Chem. Eng. J.* **2020**, *390*, 124616. [CrossRef]
93. Hu, J.; Chen, D.; Li, N.; Xu, Q.; Li, H.; He, J.; Lu, J. 3D Aerogel of Graphitic Carbon Nitride Modified with Perylene Imide and Graphene Oxide for Highly Efficient Nitric Oxide Removal under Visible Light. *Small* **2018**, *14*, 1800416. [CrossRef] [PubMed]
94. Fu, M.; Hu, X.; Wang, C.; Lu, P.; Bai, J.; Wang, R.; Tan, X. Constructing a novel NaLa $(WO4)_2$/g-C_3N_4 Z-scheme heterojunction with efficient carrier separation for excellent photocatalytic purification of NO. *J. Alloys Compd.* **2022**, *906*, 164371. [CrossRef]
95. Wang, H.; Zhang, Q.; Yang, Y.; Bian, J.; Li, C. Photocatalytic oxidation of high concentration NO over SnS_2/g-C_3N_4: A mechanistic study. *J. Fuel Chem. Techn.* **2025**, *53*, 323–334. [CrossRef]
96. Li, H.; Wu, X.; Yin, S.; Katsumata, K.; Wang, Y. Effect of rutile TiO_2 on the photocatalytic performance of g-C_3N_4/brookite-$TiO_{2-x}N_y$ photocatalyst for NO decomposition. *Appl. Surf. Sci.* **2017**, *392*, 531–539. [CrossRef]
97. Li, Y.; Lv, K.; Ho, W.; Dong, F.; Wu, X.; Xia, Y. Hybridization of rutile TiO_2 ($rTiO_2$) with g-C_3N_4 quantum dots (CN QDs): An efficient visible-light-driven Z-scheme hybridized photocatalyst. *Appl. Catal. B* **2017**, *202*, 611–619. [CrossRef]
98. Zhang, J.; Tao, H.; Wu, S.; Yang, J.; Zhu, M. Enhanced durability of nitric oxide removal on TiO_2 (P25) under visible light: Enabled by the direct Z-scheme mechanism and enhanced structure defects through coupling with C_3N_5. *Appl. Catal. B* **2021**, *296*, 120372. [CrossRef]
99. Li, X.; Chen, D.; Li, N.; Xu, Q.; Li, H.; He, J.; Lu, J. One-Step Synthesis of Honeycomb-Like Carbon Nitride Isotype Heterojunction as Low-Cost, High-Performance Photocatalyst for Removal of NO. *ACS Sustain. Chem. Eng.* **2018**, *6*, 11063–11070. [CrossRef]
100. Vinh, T.H.T.; Thi, C.M.; Van Viet, P. Enhancing photocatalysis of NO gas degradation over g-C_3N_4 modified α-Bi_2O_3 microrods composites under visible light. *Mater. Lett.* **2020**, *281*, 128637. [CrossRef]
101. Van Viet, P.; Nguyen, H.-P.; Tran, H.-H.; Bui, D.-P.; Hai, L.V.; Pham, M.-T.; You, S.-J.; Thi, C.M. Constructing g-C_3N_4/SnO_2 S-scheme heterojunctions for efficient photocatalytic NO removal and low NO_2 generation. *J. Sci. Adv. Mater. Dev.* **2021**, *6*, 551–559. [CrossRef]
102. Pham, M.-T.; Tran, D.P.H.; Pham, V.V.; Nguyen, P.H.; Nguyen, M.-K.; Kogularasu, S.; Huynh, L.T.N.; Lee, Y.-Y.; Chang-Chien, G.-P.; Chang, T.-C.; et al. Investigating the role of Pd-coated TiO_2@g-C_3N_4 heterojunctions in enhancing photocatalytic NO removal. *FlatChem* **2025**, *52*, 100898. [CrossRef]
103. Ren, Y.; Li, Y.; Wu, X.; Wang, J.; Zhang, G. S-scheme Sb_2WO_6/g-C_3N_4 photocatalysts with enhanced visible-light-induced photocatalytic NO oxidation performance. *Chin. J. Catal.* **2021**, *42*, 69–77. [CrossRef]
104. Hossain, S.M.; Park, H.; Kang, H.-J.; Mun, J.S.; Tijing, L.; Rhee, I.; Kim, J.-H.; Jun, Y.-S.; Shon, H.K. Synthesis and NO_x removal performance of anatase S-TiO_2/g-CN heterojunction formed from dye wastewater sludge. *Chemosphere* **2021**, *275*, 130020. [CrossRef]
105. Li, K.; Cui, W.; Li, J.; Sun, Y.; Chu, Y.; Jiang, G.; Zhou, Y.; Zhang, Y.; Dong, F. Tuning the reaction pathway of photocatalytic NO oxidation process to control the secondary pollution on monodisperse Au nanoparticles@g-C_3N_4. *Chem. Eng. J.* **2019**, *378*, 122184. [CrossRef]
106. Geng, J.; Zhao, L.; Wang, M.; Dong, G.; Ho, W. The photocatalytic NO-removal activity of g-C_3N_4 significantly enhanced by the synergistic effect of Pd^0 nanoparticles and N vacancies. *Environ. Sci. Nano* **2022**, *9*, 742–750. [CrossRef]

107. Jiang, G.; Li, X.; Lan, M.; Shen, T.; Lv, X.; Dong, F.; Zhang, S. Monodisperse bismuth nanoparticles decorated graphitic carbon nitride: Enhanced visible-light-response photocatalytic NO removal and reaction pathway. *Appl. Catal. B* **2017**, *205*, 532–540. [CrossRef]
108. Fan, Q.; Yan, Z.; Li, J.; Xiong, X.; Li, K.; Dai, G.; Jin, Y.; Wu, C. Interfacial-electric-field guiding design of a Type-I $FeIn_2S_4$@$ZnIn_2S_4$ heterojunction with ohmic-like charge transfer mechanism for highly efficient solar H_2 evolution. *Appl. Surf. Sci.* **2024**, *663*, 160206. [CrossRef]
109. Sharma, J.; Dhiman, P.; Kumar, A.; Sharma, G. Advances in photocatalytic NO oxidation by Z-scheme heterojunctions. *Environ. Res.* **2024**, *240*, 117431. [CrossRef]
110. Zhang, L.; Zhang, J.; Yu, H.; Yu, J. Emerging S-Scheme Photocatalyst. *Adv. Mater.* **2022**, *34*, 2107668. [CrossRef]
111. Kumar, A.; Rana, S.; Wang, T.; Dhiman, P.; Sharma, G.; Du, B.; Stadler, F.J. Advances in S-scheme heterojunction semiconductor photocatalysts for CO_2 reduction, nitrogen fixation and NO_x degradation. *Mater. Sci. Semicond. Process.* **2023**, *168*, 107869. [CrossRef]

Disclaimer/Publisher's Note: The statements, opinions and data contained in all publications are solely those of the individual author(s) and contributor(s) and not of MDPI and/or the editor(s). MDPI and/or the editor(s) disclaim responsibility for any injury to people or property resulting from any ideas, methods, instructions or products referred to in the content.